

## Electronic Supplementary Information

### Stimuli-Responsive Photoswitch-Actinide Binding: A Match Made in MOFs

Kyoung Chul Park,<sup>a</sup> Jaewoong Lim,<sup>a</sup> Grace C. Thaggard,<sup>a</sup> Buddhima K. P. Maldeni Kankanamalage,<sup>a</sup> Ingrid Lehman-Andino,<sup>b</sup> Yuan Liu,<sup>c</sup> Jennii M. Burrell,<sup>a</sup> Corey R. Martin,<sup>b</sup> An T. Ta,<sup>c</sup> Andrew B. Greytak,<sup>a</sup> Jake W. Amoroso,<sup>b</sup> David D. DiPrete,<sup>b</sup> Mark D. Smith,<sup>a</sup> Simon R. Phillpot,<sup>c</sup> and Natalia B. Shustova<sup>\*a</sup>

<sup>a</sup>*University of South Carolina, Department of Chemistry and Biochemistry, Columbia, South Carolina 29201, United States*

<sup>b</sup>*Savannah River National Laboratory, Aiken, South Carolina 29808, United States*

<sup>c</sup>*University of Florida, Department of Materials Science and Engineering, Gainesville, Florida 32611, United States*

## Table of Contents

1. Experimental procedures	S4
2. Materials	S4
3. Preparation of UiO-67	S4
4. Preparation of UiO-67+SP-COOH	S5
5. Estimation of binding constants by UV-vis spectroscopic analysis	S5
6. <b>Table S1.</b> Preparation of solutions used for UV-vis spectroscopic determination of binding constants	S6
7. Estimation of the binding constant for MC- <sup>239</sup> Pu by UV-vis spectroscopic analysis	S6
8. Determination of binding stoichiometry in MC-M <sup>n+</sup> complexes by Job's plot analysis	S7
9. Control experiments performed for UV-vis spectroscopic analysis of binding constants	S7
10. Isothermal titration calorimetry experiments	S7
11. <b>Table S2.</b> Summary of thermodynamic data derived from ITC experiments	S8
12. Capture and release of Th(IV) cations by UiO-67+SP-COOH	S8
13. Diffuse reflectance spectroscopy	S9
14. General digestion procedure	S9
15. Thermogravimetric analysis	S9
16. Other physical measurements	S9
17. X-ray crystal structure refinement for MC-UO <sub>2</sub> <sup>2+</sup> (UO <sub>2</sub> (NO <sub>3</sub> ) <sub>2</sub> (H <sub>2</sub> O)(C <sub>19</sub> H <sub>18</sub> N <sub>2</sub> O <sub>2</sub> ))	S10
18. <b>Figure S1.</b> X-ray crystal structure of MC-UO <sub>2</sub> <sup>2+</sup>	S10
19. <b>Table S3.</b> X-ray structure refinement data for MC-UO <sub>2</sub> <sup>2+</sup>	S11
20. Computational details	S12
21. <b>Table S4.</b> Lowest total energies with corresponding spin multiplicities for actinide/transition metal chlorides	S13
22. <b>Table S5.</b> Optimized radii for heavy elements based on literature reports	S13
23. <b>Table S6.</b> Binding energies with various corrections under implicit solvation model	S14
24. <b>Figure S2.</b> TGA plot of UiO-67	S15
25. <b>Figure S3.</b> TGA plot of UiO-67+SP-COOH	S15
26. <b>Figure S4.</b> PXRD patterns of UiO-67 and UiO-67+SP-COOH	S16
27. <b>Figure S5.</b> <sup>1</sup> H NMR spectrum of digested UiO-67+SP-COOH	S16
28. <b>Figure S6.</b> ITC thermogram resulting from titration of EtOH with a ThCl <sub>4</sub> solution	S17
29. <b>Figure S7.</b> ITC thermogram resulting from titration of EtOH with a UCl <sub>4</sub> solution	S17
30. <b>Figure S8.</b> ITC thermogram resulting from titration of an MC solution with EtOH	S17
31. <b>Figure S9.</b> ITC thermogram resulting from titration of EtOH with EtOH	S18
32. <b>Figure S10.</b> Calibration curve for spectroscopic determination of the concentration of thorium cations in solution	S18
33. <b>Figure S11.</b> Absorbance spectra and binding constant plot for the interaction of MC and ThCl <sub>4</sub> in EtOH	S19
34. <b>Figure S12.</b> Absorbance spectra of control experiments involving titration of SP with ThCl <sub>4</sub> in the dark and titration of EtOH with ThCl <sub>4</sub>	S19
35. <b>Figure S13.</b> Absorbance spectra and binding constant plot for the interaction	S19

of MC and UCl <sub>4</sub> in EtOH	S20
<b>36. Figure S14.</b> Absorbance spectra of control experiments involving titration of SP with UCl <sub>4</sub> in the dark and titration of EtOH with UCl <sub>4</sub>	S20
<b>37. Figure S15.</b> Absorbance spectra and binding constant plot for the interaction of MC and Ce(NO <sub>3</sub> ) <sub>3</sub> in MeCN	S21
<b>38. Figure S16.</b> Absorbance spectra of control experiments involving titration of SP with Ce(NO <sub>3</sub> ) <sub>3</sub> in the dark and titration of MeCN with Ce(NO <sub>3</sub> ) <sub>3</sub>	S21
<b>39. Figure S17.</b> Absorbance spectra and binding constant plot for the interaction of MC and ZnI <sub>2</sub> in MeCN	S22
<b>40. Figure S18.</b> Absorbance spectra of control experiments involving titration of SP with ZnI <sub>2</sub> in the dark and titration of MeCN with ZnI <sub>2</sub>	S22
<b>41. Figure S19.</b> Absorbance spectra and binding constant plot for the interaction of MC and ThCl <sub>4</sub> in DMF	S23
<b>42. Figure S20.</b> Absorbance spectra of control experiments involving titration of SP with ThCl <sub>4</sub> in the dark and titration of DMF with ThCl <sub>4</sub>	S23
<b>43. Figure S21.</b> Absorbance spectra and binding constant plot for the interaction of MC and UCl <sub>4</sub> in DMF	S24
<b>44. Figure S22.</b> Absorbance spectra of control experiments involving titration of SP with UCl <sub>4</sub> in the dark and titration of DMF with UCl <sub>4</sub>	S24
<b>45. Figure S23.</b> Absorbance spectra and binding constant plot for the interaction of MC and UO <sub>2</sub> (NO <sub>3</sub> ) <sub>2</sub> in DMF	S25
<b>46. Figure S24.</b> Absorbance spectra of control experiments involving titration of SP with UO <sub>2</sub> (NO <sub>3</sub> ) <sub>2</sub> in the dark and titration of DMF with UO <sub>2</sub> (NO <sub>3</sub> ) <sub>2</sub>	S25
<b>47. Figure S25.</b> Absorbance spectra and binding constant plot for the interaction of MC and Ce(NO <sub>3</sub> ) <sub>3</sub> in DMF	S26
<b>48. Figure S26.</b> Absorbance spectra of control experiments involving titration of SP with Ce(NO <sub>3</sub> ) <sub>3</sub> in the dark and titration of DMF with Ce(NO <sub>3</sub> ) <sub>3</sub>	S26
<b>49. Figure S27.</b> Absorbance spectra and binding constant plot for the interaction of MC and NdCl <sub>3</sub> in DMF	S27
<b>50. Figure S28.</b> Absorbance spectra of control experiments involving titration of SP with NdCl <sub>3</sub> in the dark and titration of DMF with NdCl <sub>3</sub>	S27
<b>51. Figure S29.</b> Job's plot analysis of the MC–Ce <sup>3+</sup> metal complex in DMF	S28
<b>52. Figure S30.</b> Job's plot analysis of the MC–Nd <sup>3+</sup> metal complex in DMF	S28
<b>53. Figure S31.</b> Job's plot analysis of the MC–U <sup>4+</sup> metal complex in DMF	S29
<b>54. Figure S32.</b> Job's plot analysis of the MC–UO <sub>2</sub> <sup>2+</sup> metal complex in DMF	S29
<b>55. Figure S33.</b> Job's plot analysis of the MC–Th <sup>4+</sup> metal complex in DMF	S30
<b>56. Figure S34.</b> Absorbance spectra and photoisomerization kinetic studies of SP and ThCl <sub>4</sub> in EtOH	S30
<b>57. Figure S35.</b> Absorbance spectra and photoisomerization kinetic studies of SP and UCl <sub>4</sub> in EtOH	S31
<b>58. Figure S36.</b> X-ray crystal structures of UiO-67	S31
<b>59. Figure S37.</b> X-ray crystal structures of UiO-67, SP-COOH, and MC-COOH	S32
<b>60. Figure S38.</b> Photographs of MC solutions before and after the addition of ZnI <sub>2</sub> in MeCN	S32
<b>61.</b> X-ray crystal structure refinement for MC-COOH ([C <sub>20</sub> H <sub>19</sub> N <sub>2</sub> O <sub>5</sub> ]Cl)	S33
<b>62. Figure S39.</b> X-ray crystal structure of MC-COOH	S33
<b>63. Table S7.</b> X-ray structure refinement data for MC-COOH	S34
<b>64. References</b>	S34

## Experimental Procedures.

**Caution!** Uranium-, thorium-, and plutonium-containing compounds are radioactive and chemically toxic. Suitable precaution, care, and protection for the handling of such substances must be followed.

## Materials.

Zirconium chloride (99.5%, Alfa Aesar), cerium(III) nitrate hexahydrate (99.5%, Acros Organics), neodymium(III) chloride hydrate (99.9%, Alfa Aesar), zinc iodide (99+%, Acros Organics), thorium chloride (>95%, International Bio-Analytical Industries Inc.), uranium tetrachloride (>95%, International Bio-Analytical Industries Inc.), uranyl nitrate hexahydrate (98%, International Bio-Analytical Industries Inc.), 3-methyl-2-butanone (98%, BeanTown Chemical), 4,4'-biphenyldicarboxylic acid (97%, Oakwood Chemical), 4-hydrazineyl benzoic acid (98.77%, AmBeed, Inc.), methyl trifluoromethanesulfonate (97%, Matrix Scientific), 2-hydroxy-5-nitrobenzaldehyde (98%, Oakwood Chemical), glacial acetic acid (ACS grade, BDH), ethanol (200 proof, Decon Laboratories, Inc.), diethyl ether (>99%, Sigma-Aldrich), hexane (ACS grade, BDH), isopropyl alcohol (ACS grade, BDH), 1,3,3-trimethylindolino-6'-nitrobenzopyrylospiran (>98%, TCI), arsenazo (III) (>95%, TCI), hydrochloric acid (ACS, Fisher Chemical), nitric acid (ACS reagent, Sigma-Aldrich), acetone (ACS grade, Sigma-Aldrich), dichloromethane (ACS grade, Macron), pyridine (99%, BeanTown Chemical), *N,N*-dimethylformamide (ACS grade, Oakwood Chemical), acetonitrile (99.5%, Sigma-Aldrich), chloroform-*d* (99.8%, Cambridge Isotope Laboratories, Inc.), and dimethyl sulfoxide-*d*<sub>6</sub> (99.9%, Cambridge Isotope Laboratories, Inc.) were used as received. The Savannah River National Laboratory (SRNL) was used as the supplier of the <sup>239</sup>Pu and <sup>243</sup>Am isotopes, including <sup>239</sup>Pu(NO<sub>3</sub>)<sub>4</sub> and <sup>243</sup>Am(NO<sub>3</sub>)<sub>3</sub>, and the corresponding experiments have also been carried out at the SRNL designated transuranic laboratory.

The compounds 1',3',3'-trimethyl-6-nitrospiro[chromene-2,2'-indoline]-5'-carboxylic acid (SP-COOH)<sup>[1]</sup> and Zr<sub>6</sub>O<sub>4</sub>(OH)<sub>4</sub>(BPDC)<sub>6</sub> (H<sub>2</sub>BPDC = [1,1'-biphenyl]-4,4'-dicarboxylic acid: UiO-67; UiO = University of Oslo)<sup>[2]</sup> were synthesized based on modified literature procedures.

## Preparation of UiO-67.

In a 20-mL vial, ZrCl<sub>4</sub> (67.0 mg, 288 μmol) and H<sub>2</sub>BPDC (90.0 mg, 372 μmol) were dissolved in 15 mL of *N,N*-dimethylformamide (DMF), and 1.00 mL of HCl was added. The resulting mixture was sonicated for 10 minutes and then heated in an oven at 80 °C for 24 hours. After cooling to room temperature, the resulting powder was collected by filtration and washed with DMF (3 × 10 mL) and ethanol (EtOH, 3 × 10 mL). To increase the average number of defects per metal node in UiO-67, 30.0 mg of freshly synthesized UiO-67 was exposed to 15 mL of acetonitrile (MeCN) in a 20-mL vial, and the resulting mixture was heated in a heating block at 55 °C for three days. After cooling to room temperature, the acquired powder was collected by filtration and washed with MeCN (3 × 10 mL) and EtOH (3 × 10 mL). The number of defects per metal node was carefully evaluated for each batch using thermogravimetric analysis (TGA) according to a literature procedure, resulting in an average of four defects per metal node (Figure S2).<sup>[3]</sup> The crystallinity of UiO-67 was assessed by powder X-ray diffraction (PXRD) analysis, as shown in Figure S4. The crystalline powders of Zr<sub>6</sub>O<sub>4</sub>(OH)<sub>8</sub>(BPDC)<sub>4</sub> (73.1 mg, 42.8 μmol) were isolated in 89% yield.

### **Preparation of UiO-67+SP-COOH.**

To postsynthetically integrate SP-COOH in UiO-67, parent UiO-67 was first synthesized according to the modified literature procedure described above.<sup>[1]</sup> Then, the UiO-67 powder was collected by filtration, thoroughly washed with DMF ( $3 \times 10$  mL), and then dried in air for 10 minutes. After drying, UiO-67 (25.0 mg, 14.6  $\mu$ mol) was placed in a 1-dram vial. Then, 1.00 mL of a 60.0 mM DMF solution of SP-COOH was added. The vial containing the resulting mixture was placed in a preheated aluminum block at 75 °C for 72 hours. After cooling to room temperature, the resulting powder was collected by filtration and washed with DMF ( $3 \times 10$  mL). The PXRD patterns of parent UiO-67 and UiO-67+SP-COOH are shown in Figure S4. PXRD studies confirmed that MOF crystallinity was preserved after postsynthetic linker installation (Figure S4). The amount of SP-COOH installed in UiO-67 was calculated using a combination of TGA of the parent MOF and <sup>1</sup>H NMR spectroscopic analysis of the digested UiO-67+SP-COOH sample, which corresponds to 0.9 of SP-COOH integrated per metal node. The <sup>1</sup>H NMR spectrum of the digested MOF sample confirming the integration of SP-COOH is shown in Figure S5.

### **Estimation of binding constants by UV-vis spectroscopic analysis.**

In order to spectroscopically determine the binding constants between a spiropyran derivative, 1,3,3-trimethylindolino-6'-nitrobenzopyrlospiran (SP), and various metal cations, 10 mM stock solutions of SP in organic solvents (e.g., EtOH, DMF, and MeCN) were first prepared. Next, stock solutions of each metal salt (1–10 mM, Table S1) were prepared in the same organic solvents. As a reference point, the absorbance spectrum of merocyanine in the absence of metal salts was first collected by diluting aliquots (either 5 or 10  $\mu$ L, Table S1) of the SP stock solution to a total volume of 2.0 mL in a 1.0-cm quartz cuvette. Prior to collecting the absorbance spectrum, the diluted SP solution was exposed to a 365-nm excitation wavelength for three minutes to promote photoisomerization to the merocyanine isomer, and the cuvette was then immediately transferred to the UV-vis spectrometer for analysis. In every case, the characteristic absorbance band corresponding to the merocyanine centered around 530–570 nm was detected (Figures S11, S13, S15, S17, S19, S21, S23, S25, and S27). The quartz cuvette was then cleaned three times with acetone before analyzing subsequent samples. Next, the binding interactions between merocyanine and various metal cations were evaluated by adding varying equivalents of metal salt (0.00–10000 equivalents with respect to a photochromic derivative; Table S1) using the prepared stock solutions. After mixing the SP and metal salt solutions in the quartz cuvette, the sample was again exposed to a 365-nm excitation wavelength for three minutes to promote binding of the metal cations by merocyanine. After three minutes of irradiation at 365 nm, the cuvette was immediately transferred to the UV spectrometer for analysis. Importantly, every sample was exposed to UV light ( $\lambda_{\text{ex}} = 365$  nm) for the same amount of time at a consistent distance to ensure that any changes in the intensity of the merocyanine absorbance were due to complex formation, not attenuation of merocyanine to SP. To determine the concentration of metal cations bound by merocyanine, the intensity of the band from 530–570 nm, corresponding to free merocyanine, was monitored. The binding constants were estimated based on the acquired UV-vis data using a modified Benesi-Hildebrand equation (main text). The full experimental details, including choice of solvent, metal salt, number of equivalents of metal salt versus SP, and the estimated binding constants, are given below in Table S1. The corresponding UV-vis absorbance spectra are given in Figures S11, S13, S15, S17, S19, S21, S23, S25, and S27.

**Table S1.** Preparation of solutions used for UV-vis spectroscopic determination of binding constants.

metal salt (concentration)	solvent	aliquot of SP stock solution, $\mu\text{L}$	metal cation equivalents	$K_a, \text{M}^{-1}$
$\text{ThCl}_4$ (2 mM)	EtOH	10	0.00–0.50	$8.8 \pm 3.4 \times 10^4$
$\text{UCl}_4$ (10 mM)	EtOH	10	0.00–0.40	$1.3 \pm 0.5 \times 10^5$
$\text{Ce}(\text{NO}_3)_3 \cdot 6\text{H}_2\text{O}$ (10 mM)	MeCN	5	0.00–2.0	$2.3 \pm 1.2 \times 10^5$
$\text{ZnI}_2$ (1 mM)	MeCN	5	0.00–2.0	$6.5 \pm 0.5 \times 10^4$
$\text{ThCl}_4$ (10 mM)	DMF	5	0.00–100	$7.3 \pm 0.8 \times 10^3$
$\text{UCl}_4$ (10 mM)	DMF	5	0.00–20	$5.8 \pm 0.6 \times 10^3$
$\text{UO}_2(\text{NO}_3)_2 \cdot 6\text{H}_2\text{O}$ (10 mM)	DMF	5	0.00–50	$5.3 \pm 1.1 \times 10^3$
$\text{Pu}(\text{NO}_3)_4$ (1 mM)	DMF	10	0.00–1.6	$4.3 \times 10^4$
$\text{Ce}(\text{NO}_3)_3 \cdot 6\text{H}_2\text{O}$ (10 mM)	DMF	5	0.00–10000	$2.1 \pm 0.6 \times 10^4$
$\text{NdCl}_3 \cdot \text{H}_2\text{O}$ (10 mM)	DMF	5	0.00–20	$5.2 \pm 0.5 \times 10^4$

#### Estimation of the binding constant for $^{239}\text{Pu}$ by UV-vis spectroscopic analysis.

The plutonium(IV) solution used for the determination of the binding constant with MC by UV-vis spectroscopy was prepared at SRNL using the following procedure. An aliquot of 1.30 mL of a stock solution of  $^{239}\text{Pu}(\text{NO}_3)_4$  ( $1.05 \times 10^7$  Bq/mL) in nitric acid was added to 10.0 mL of 4 M nitric acid. The sample was purified using a TEVA column cartridge and eluted with a mixture of nitric acid (0.02 M) and hydrofluoric acid (0.02 M). The resulting eluent was heated to evaporate the solvent mixture to yield  $^{239}\text{Pu}(\text{NO}_3)_4$  as a solid. Solid  $^{239}\text{Pu}(\text{NO}_3)_4$  was then redissolved in 4.00 mL of DMF, resulting in a stock solution of  $^{239}\text{Pu}(\text{NO}_3)_4$  ( $1.13 \times 10^6$  Bq/mL). The prepared stock solution (0.200 mL) was diluted in 0.800 mL of DMF to be used as a titrant in the following experiment. UV-vis spectroscopy experiments using the prepared  $^{239}\text{Pu}(\text{NO}_3)_4$  titrant were carried out using an Ocean Insight (Ocean-HDX-UV-VIS) optimized spectrometer. For this, a background spectrum of pure DMF was first collected. Then, in a 1.0-mL quartz semi-micro cuvette (path length = 1.0 cm), 10.0  $\mu\text{L}$  of a stock solution of SP in DMF (1 mM) was diluted to a total volume of 0.700 mL. The cuvette was then irradiated with a 365-nm excitation wavelength for three minutes prior to collecting the initial absorbance spectrum of the merocyanine isomer. Next, varying equivalents of  $^{239}\text{Pu}(\text{NO}_3)_4$  were added to the SP solution (0.00–1.6 equivalents with respect to SP) by adding aliquots of the  $^{239}\text{Pu}(\text{NO}_3)_4$  titrant solution according to Table S1. The cuvette was cleaned and dried in between each measurement. To determine the concentration of metal cations bound by merocyanine, the intensity of the band around 565 nm, corresponding to free merocyanine, was monitored. The binding constants were estimated based on the acquired UV-vis data using a modified Benesi-Hildebrand equation (main text). The full experimental details, including choice of solvent, metal salt, number of equivalents of metal salt versus SP, and the estimated binding constants, are given below in Table S1. The corresponding UV-vis absorbance spectra are given in Figure 5 of the main text.

### **Determination of binding stoichiometry for MC-based metal complexes by Job's plot analysis.**

In order to evaluate the preferred binding stoichiometry for MC–M<sup>n+</sup> complexes in solution, Job's plot analysis was performed using UV-vis spectroscopic data based on a literature procedure.<sup>[4]</sup> For this, a series of 10–15 solutions containing varying molar ratios of SP and each metal salt were prepared by diluting 10 mM stock solutions of SP and metal salt, where the mole fraction of the metal salt ranged from 0.0–1.0. In each case, the total volume of the solution was set to be 2.0 mL. Next, the absorbance of each solution was analyzed by UV-vis spectroscopy, and the band between 430–450 nm, corresponding to the MC–M<sup>n+</sup> complex, was monitored as a function of the mole fraction of the metal salt. The binding stoichiometry for each MC-metal complex was determined by plotting the absorbance of the solutions at 450 nm as a function of the mole fraction of the metal salt. The mole fraction at which the maximum absorbance was reached was taken as the ideal ratio for complex formation. The corresponding Job's plots and MC–M<sup>n+</sup> complex binding stoichiometries are given in Figures 4 and S29–S33.

### **Control experiments performed for UV-vis spectroscopic analysis of binding constants.**

In order to ensure that the detected changes in the absorbance spectra of SP and metal salt solutions were accurately attributed to the formation of MC–M<sup>n+</sup> complexes, two types of control experiments were performed. The first control experiment was designed to evaluate whether the closed spiropyran photoisomer, as opposed to the merocyanine isomer, was capable of metal cation chelation. For this, 10- $\mu$ L aliquots of a 10 mM solution of SP in either EtOH, DMF, or MeCN were diluted to a total volume of 2.0 mL in a quartz cuvette. Next, the initial absorbance profile of the diluted SP solution was collected without exposure to a 365-nm excitation wavelength (i.e., without promotion of spiropyran-to-merocyanine photoisomerization). The possible binding interactions between spiropyran and various metal cations were then evaluated by adding varying equivalents of metal salt (0.00–10000 equivalents with respect to SP, Table S1) using the prepared stock solutions. The UV-vis spectrum of the spiropyran and metal salt solution was collected after each addition of metal salt, showing no significant change in the absorbance profile with increasing metal salt concentration. As a result, the spiropyran isomer is unlikely to contribute to complex formation. The second control experiment was performed in order to rule out the possibility that the metal salt solutions themselves were contributing to the changes in the absorbance profiles of the MC–M<sup>n+</sup> complex solutions. In this direction, the UV-vis absorbance spectra of each metal salt solution were collected using the same molar concentration as was used to determine the binding constants for MC–M<sup>n+</sup> complexes. As a result, we detected no changes in absorbance based on the concentration of the metal salt in the absence of spiropyran. The UV-vis absorbance spectra for all control experiments are given in Figures S12, S14, S16, S18, S20, S22, S24, S26, and S28.

### **Isothermal titration calorimetry (ITC) experiments.**

The binding constants between MC and either uranium or thorium were measured using isothermal titration calorimetry (ITC) experiments performed on a TA Instruments Affinity ITC under air at 25 °C. As the instrument is typically kept under aqueous conditions, a system transfer to EtOH was performed by rinsing the titrant syringe, sample cell, and reference cell with EtOH at least six times. Several EtOH–EtOH control experiments were subsequently carried out to allow the instrument to equilibrate with the organic solvent system and to verify repeatable instrumental responses before collecting the reported experimental data. Moreover, selection of EtOH as the solvent was done considering the solubility of all analytes (metal salts and SP) to prevent

precipitation in the sample cell. The metal salt solutions (0.25 mM) were titrated from a 0.150 mL syringe into a gold sample cell containing 0.350 mL of a 1 mM solution of SP in EtOH. The total active cell volume was 185  $\mu$ L. The power compensation required to maintain the sample cell at 25  $^{\circ}$ C (relative to a reference cell filled with an equal volume, 0.350 mL, of pure EtOH) was monitored over time with each injection. All experiments allowed for a mid-range power variation. Each injection was followed by a 200-s interval to allow proper equilibration between metal salt injections, with a total of 30 injections of 2.50  $\mu$ L each. The cell contents were stirred continuously at 150 rpm over the course of the titration. In order to target quantification of binding interactions between uranium and thorium with the merocyanine (MC) isomer, the SP solution in EtOH was irradiated with UV light ( $\lambda_{\text{ex}} = 365$  nm) for 10 minutes prior to loading it into the sample cell and beginning the experiment. Reference titrations of EtOH-to-EtOH and EtOH to irradiated MC solution were conducted under identical parameters as the metal-to-SP titrations. Notably, the thermal signal of the control titrations was insignificant in comparison with the thermal signal produced by MC– $M^{n+}$  binding interactions (Figures S6–S9). The sample cell and titrant syringe were thoroughly cleaned with EtOH before each titration experiment. The resulting baseline-corrected thermograms are given in Figure 2 of the main text. The raw heat signals, represented in the thermograms, were then fit with a Langmuir model describing binding at identical independent sites (Figure 2, main text) to estimate the corresponding binding constants.

**Table S2.** Summary of thermodynamic data derived from ITC experiments.

metal salt	solvent	$\Delta G$ , kJ/mol	$\Delta H$ , kJ/mol	$\Delta S$ , J/mol·K	$K_a$ , $M^{-1}$
ThCl <sub>4</sub>	EtOH	–28.31	–56.47	–94.46	$9.1 \times 10^4$
UCl <sub>4</sub>	EtOH	–30.08	–98.45	–229.3	$1.9 \times 10^5$

### Capture and release of Th(IV) cations by UiO-67+SP-COOH.

In order to evaluate the possible capture and release of radionuclides by UiO-67+SP-COOH in response to an excitation wavelength, 2.00 mg of UiO-67+SP-COOH (0.989  $\mu$ mol) was first placed in a 1-dram vial. Next, 3.00 mL of a thorium nitrate solution (19.4 mM in DMF) was added to the vial containing UiO-67+SP-COOH. The samples were then heated at 75  $^{\circ}$ C in an oven for five days to promote diffusion of the thorium cations throughout the MOF pores followed by equilibration with the surrounding solution. After 120 hours, the resulting Th@UiO-67+SP-COOH suspension was irradiated with a 590-nm excitation wavelength for one hour to promote the formation of the closed SP isomer. Then, an aliquot (2.00  $\mu$ L) of the supernatant was collected and placed directly into a 1.0-cm quartz cuvette, with special attention not to remove any suspended particles. The aliquots were diluted with DMF to 0.100 mL inside the 1.0-cm quartz cuvette. The samples were then diluted to a final volume of 3.0 mL with a  $3.30 \times 10^{-5}$  M complexing solution of arsenazo (III) in H<sub>2</sub>O and subsequently analyzed using UV-vis spectroscopy to determine the initial concentration of thorium cations in the supernatant. Next, the Th@UiO-67+SP-COOH suspension was irradiated with a 365-nm excitation wavelength for 10 minutes to promote the formation of the MC isomer to bind thorium cations. Again, an aliquot of the supernatant solution was analyzed as described before to determine the concentration of thorium cations in the supernatant after exposure to UV light. To quantify the amount of thorium cations, present in the supernatant solution, a calibration curve was constructed with known concentrations of DMF, H<sub>2</sub>O, and thorium nitrate in the presence of arsenazo (III) (Figure S10). To determine the concentration

of thorium cations, the intensity of the band centered at 667 nm, corresponding to the arsenazo (III)-thorium complex, was monitored.

### **Diffuse reflectance spectroscopy.**

In order to evaluate the photoresponsive behavior of UiO-67+SP-COOH, time-resolved diffuse reflectance spectroscopic studies were conducted using an Ocean Optics JAZ spectrometer. An Ocean Optics ISP-REF integrating sphere was connected to the spectrometer using a 450- $\mu\text{m}$  SMA fiber optic cable. Samples were loaded in a 4.0-mm quartz sample cell that was referenced to an Ocean Optics WS-1 Spectralon<sup>®</sup> standard. A mounted high-powered LED (M365L2, Thorlabs,  $\lambda_{\text{ex}}$  = 365 nm, distance = 2.5 cm, and LEDD1B power supply set at 700 mA) was used for *in situ* irradiation of the samples. In all cases, a 400-nm longpass glass filter (Thorlabs, FGL400) was placed between the quartz sample holder and the integrating sphere to filter any UV light from the internal tungsten-halogen lamp. The quartz sample holder and longpass filter were attached to the top of the integrating sphere with electrical tape to prevent sample displacement.

### **General digestion procedure.**

For analysis by <sup>1</sup>H NMR spectroscopy, UiO-67 samples with integrated photochromic molecules (2.00 mg) were transferred to a 20-mL vial and treated with 50.0  $\mu\text{L}$  of D<sub>2</sub>SO<sub>4</sub>. The resulting solution was then diluted with 0.500 mL of DMSO-*d*<sub>6</sub>. The samples were then sonicated for 10 minutes to ensure complete dissolution before being transferred to NMR tubes for analysis. The <sup>1</sup>H NMR spectrum of digested samples is shown in Figure S5.

### **Thermogravimetric analysis.**

TGA was used to determine the thermal stability of the synthesized UiO-67 and to estimate the number of defects per metal node in the synthesized samples.<sup>[3]</sup> TGA was performed on an SDT Q600 thermogravimetric analyzer. Samples were loaded inside an alumina boat as the sample holder at a heating rate of 5 °C/minute to 600 °C under 10 mL/minute airflow. A significant weight loss was observed during heating above 400 °C (Figures S2 and S3), which was used to calculate the number of defects per metal node based on a literature procedure.<sup>[3]</sup>

### **Other physical measurements.**

<sup>1</sup>H NMR spectra were collected on a Bruker Avance III-HD 400 MHz NMR spectrometer and referenced to the residual <sup>1</sup>H peak of DMSO-*d*<sub>6</sub> (2.50 ppm). PXRD patterns were recorded on a Rigaku Miniflex 6G diffractometer at a scan rate of 10 °/minute with accelerating voltage and current of 40 kV and 15 mA, respectively. UV-vis was recorded using a ThermoFisher Evolution 350 UV-vis spectrometer equipped with Thermo Insight software. Samples for UV-vis were prepared directly in the 1.0-cm quartz cuvettes for all measurements. Gamma-ray spectroscopy was performed on diluted samples using a CANBERRA High Purity Germanium (HPGe) well detector, and columns were analyzed using a low energy germanium (LEGe) detector. An aliquot of the supernatant (0.2 mL, DMF) was diluted with 1.8 mL of distilled water and analyzed using one of several semi-planar HPGe spectrometers for the characteristic <sup>243</sup>Am 59.54 keV decay gamma rays. Sample analysis was conducted for 1800 seconds each and 1000 seconds for the dry columns in the LEGe. The statistical uncertainties were  $\leq 5\%$  for the <sup>243</sup>Am activity measurements. The spectrometers were calibrated with NIST traceable standards. Signals from the HPGe and LEGe detectors were transferred to a Lynx digital signal analyzer made by CANBERRA, and spectral data were recorded on a PC.

**X-ray crystal structure refinement for MC-UO<sub>2</sub><sup>2+</sup> complex (UO<sub>2</sub>(NO<sub>3</sub>)<sub>2</sub>(H<sub>2</sub>O)(C<sub>19</sub>H<sub>18</sub>N<sub>2</sub>O<sub>2</sub>)).** X-ray intensity data from an orange platelike single crystal were collected at 100(2) K using a Bruker D8 QUEST diffractometer equipped with a PHOTON-II area detector and an Incoatec microfocus source (Mo K<sub>α</sub> radiation, λ = 0.71073 Å). The raw area detector data frames were reduced, scaled, and corrected for absorption effects using the Bruker APEX3, SAINT+, and SADABS programs.<sup>[5,6]</sup> The structure was solved using SHELXT.<sup>[7,8]</sup> Subsequent difference Fourier calculations and full-matrix least-squares refinement against *F*<sup>2</sup> were performed with SHELXL-2019/3<sup>[7,8]</sup> using OLEX2.<sup>[9]</sup>

The compound crystallizes in the triclinic system. The space group *P*-1 (No. 2) was confirmed by the structure solution. The asymmetric unit consists of one complex. All non-hydrogen atoms were refined with anisotropic displacement parameters. Hydrogen atoms bonded to carbon were located in difference Fourier maps before being placed in geometrically idealized positions and included as riding atoms with *d*(C-H) = 0.95 Å and *U*<sub>iso</sub>(H) = 1.2*U*<sub>eq</sub>(C) for arene hydrogen atoms and *d*(C-H) = 0.98 Å and *U*<sub>iso</sub>(H) = 1.5*U*<sub>eq</sub>(C) for methyl hydrogens. The methyl hydrogen atoms were allowed to rotate as a rigid group to the orientation of maximum observed electron density. The two water hydrogen atoms were located and refined isotropically, with their O-H distances restrained to be similar (SHELX SADI). The largest residual electron density peak in the final difference map is 1.40 e<sup>-</sup>/Å<sup>3</sup>, located 1.04 Å from the uranium atom.

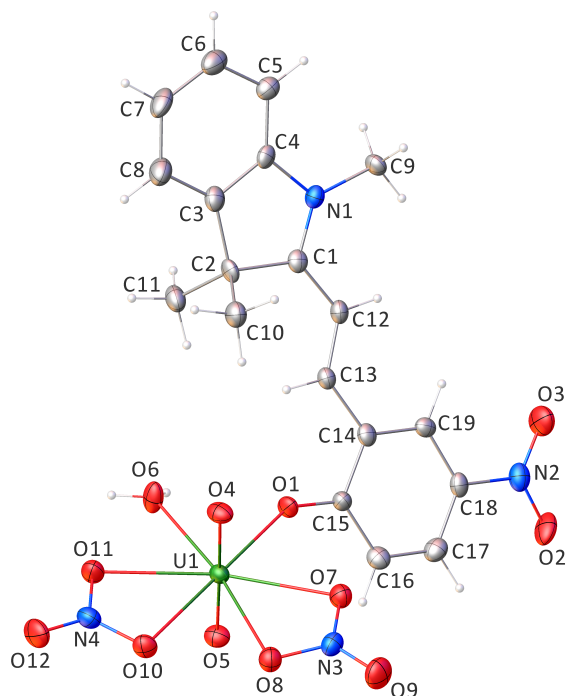


**Figure S1.** X-ray crystal structure of MC-UO<sub>2</sub><sup>2+</sup> (UO<sub>2</sub>(NO<sub>3</sub>)<sub>2</sub>(H<sub>2</sub>O)(C<sub>19</sub>H<sub>18</sub>N<sub>2</sub>O<sub>2</sub>)). Displacement ellipsoids are drawn at the 50% probability level.

**Table S3.** X-ray structure refinement data for MC-UO<sub>2</sub><sup>2+</sup> (UO<sub>2</sub>(NO<sub>3</sub>)<sub>2</sub>(H<sub>2</sub>O)(C<sub>19</sub>H<sub>18</sub>N<sub>2</sub>O<sub>2</sub>)).

compound	MC-UO <sub>2</sub> (NO <sub>3</sub> ) <sub>2</sub>
formula	C <sub>19</sub> H <sub>20</sub> N <sub>4</sub> O <sub>12</sub> U
FW, g·mol <sup>-1</sup>	734.42
<i>T</i> , K	100(2)
crystal system	triclinic
space group	<i>P</i> -1
<i>Z</i>	4
<i>a</i> , Å	10.8763(4)
<i>b</i> , Å	10.8816(4)
<i>c</i> , Å	11.2207(4)
<i>α</i> , °	106.7650(10)
<i>β</i> , °	113.8720(10)
<i>γ</i> , °	92.5920(10)
<i>V</i> , Å <sup>3</sup>	1142.70(7)
<i>d</i> <sub>calc</sub> , g cm <sup>-3</sup>	2.134
<i>μ</i> , mm <sup>-1</sup>	7.176
F(000)	784.0
crystal size, mm <sup>3</sup>	0.12 × 0.08 × 0.04
2 theta range	3.978 to 55.078
index ranges	-14 ≤ <i>h</i> ≤ 14 -14 ≤ <i>k</i> ≤ 14 -14 ≤ <i>l</i> ≤ 14
reflections collected	44146
data/restraints/parameters	5262/1/337
GOF on <i>F</i> <sup>2</sup>	1.313
largest peak/hole, e/Å <sup>3</sup>	1.40/-2.13
<i>R</i> <sub>1</sub> ( <i>wR</i> <sub>2</sub> ), %, [ <i>I</i> ≥ 2σ( <i>I</i> )] <sup>b</sup>	0.0322 (0.0944)

<sup>a</sup>Mo-K<sub>α</sub> (λ = 0.71073 Å) radiation

<sup>b</sup>
$$R_1 = \frac{\sum ||F_o| - |F_c||}{\sum |F_o|}, wR_2 = \frac{-\sum [w(F_o^2 - F_c^2)^2]}{\sum [w(F_o^2)^2]}^{1/2}$$

## Computational details.

*Binding energy equation.* To model the binding interaction between merocyanine and chloride salts of actinides or transition metals in aqueous solution at room temperature, we calculated the Gibbs free energy for merocyanine, the actinide/transition metal chlorides, and the resulting complex individually. The Gibbs free energy in aqueous solution at 298.15 K is computed using Equation S1:

$$G_{298.15\text{ K}, \text{liquid}} = E_{0\text{ K}, \text{gas}} + \Delta E_{0\text{ K} \rightarrow 298.15\text{ K}} + \Delta E_{\text{gas} \rightarrow \text{liquid}} + \Delta E_{\text{solvation}} \quad (\text{Eq. S1})$$

where  $G_{298.15\text{ K}, \text{liquid}}$  represents the total Gibbs free energy of the species at 298.15 K in solution,  $E_{0\text{ K}, \text{gas}}$  is the total energy in vacuum at 0 K,  $\Delta E_{0\text{ K} \rightarrow 298.15\text{ K}}$  is the thermal correction to the Gibbs free energy from 0 K to 298.15 K, and  $\Delta E_{\text{gas} \rightarrow \text{liquid}}$  is the energy change from the gas phase to the liquid phase at 298.15 K. In this study, we assume a 1 atm concentration for gas-phase species transforming into the 1 M concentration in the liquid phase, corresponding to an ideal gas at room temperature with a volume of 24.5 L, resulting in  $\Delta E_{\text{gas} \rightarrow \text{liquid}}$  being set to  $-1.89\text{ kcal/mol}$ ,<sup>[10]</sup> as calculated using Equation S2:

$$\Delta E_{\text{gas} \rightarrow \text{liquid}} = -RT \ln(24.5) \quad (\text{Eq. S2})$$

The final term,  $\Delta E_{\text{solvation}}$ , represents the solvation free energy.

Once the Gibbs free energy of each species is determined, the overall change in Gibbs free energy for the binding interaction between spiropyran and actinide or transition metal chlorides is calculated using Equation S3.

$$\Delta G_{298.15\text{ K}, \text{liquid}} = G_{\text{complex}} - (G_{\text{merocyanine}} + G_{\text{metal chloride}}) \quad (\text{Eq. S3})$$

Where,  $G_{\text{complex}}$  is the total Gibbs free energy of the merocyanine complex with actinide or transition metal chlorides, while  $G_{\text{merocyanine}}$  and  $G_{\text{metal chloride}}$  are the total Gibbs free energies of merocyanine and the actinide/transition metal chlorides, respectively.

*Density Functional Theory Parameter Settings.* To calculate the vacuum energy at 0 K, denoted as  $E_{0\text{ K}, \text{gas}}$ , we initially employ the TPSSh<sup>[11,12]</sup> functional in combination with the 6-311G\* basis set<sup>[13,14]</sup> for H, C, N, O, Cl, and I, and the relativistic small-core Stuttgart basis set<sup>[13,14]</sup> for heavy elements (Th, U, and Pu) to achieve structural relaxation, using Gaussian 16.<sup>[15]</sup> To account for van der Waals interactions, the DFT+D3<sup>[16,17]</sup> dispersion correction is applied. The TPSSh functional is chosen based on recommendations by Aebersold et al.<sup>[18]</sup> for calculations involving actinide elements. Due to challenges in electronic energy convergence, the quadratically convergent procedure is applied to enhance convergence. Subsequently, to obtain a more accurate electronic total energy, we use the optimized structure to perform single-point calculations with the PWPB95<sup>[19]</sup> functional combined with the def2-TZVP basis set, using ORCA.<sup>[20]</sup>

Additionally, due to the presence of unpaired electrons in the heavy elements, some calculations are performed as open-shell calculations to ensure that the actinide or transition metal chlorides are in their ground state.<sup>[21,22]</sup> To determine the ground state, we identify the configuration with the lowest total energy. In Gaussian, the spin multiplicity, specified as  $2S+1$  (where S represents the number of unpaired electrons divided by 2), is indicated in the input script. A multiplicity of 1

represents a singlet state (all electrons paired), 2 indicates a doublet (one unpaired electron), 3 corresponds to a triplet (two unpaired electrons), and so on. Table S4 below displays the lowest total energy and corresponding electron multiplicities for each compound.

**Table S4.** Lowest total energies with corresponding spin multiplicities for actinide/transition metal chlorides.

compound	multiplicity
ThCl <sub>4</sub>	1
UO <sub>2</sub> Cl <sub>2</sub>	1
PuCl <sub>4</sub>	5

The thermal correction to Gibbs free energy, denoted as  $\Delta E_{0\text{ K}\rightarrow 298.15\text{ K}}$ , is calculated using the “freq” keyword in Gaussian 16 to obtain the correction energy following structural relaxation.

For the solvation energy, an implicit solvation model via the SMD<sup>[23]</sup> method is applied, as the M052X/6-31G\* approach has been identified as optimal for this purpose.<sup>[24]</sup> The solvation energy,  $\Delta E_{\text{solvation}}$ , is calculated as follows:

$$\Delta E_{\text{solvation}} = E_{\text{M052X/6-31G}^*}^{\text{sol}} - E_{\text{M052X/6-31G}^*}^{\text{vac}} \quad (\text{Eq. S4})$$

where  $\Delta E_{\text{solvation}}$  represents the solvation energy,  $E_{\text{M052X/6-31G}^*}^{\text{vac}}$  is the total energy using the M052X/6-31G\* method in the vacuum, and  $E_{\text{M052X/6-31G}^*}^{\text{sol}}$  is the total energy calculated with the M052X/6-31G\* method under the SMD solvation model.

However, since there is no parameterization available for heavy elements in the SMD method, we referred to values provided in the previous literature, which offer optimized radii for heavy elements, and used these values in our calculations. The results are presented in Table S5 below.

**Table S5.** Optimized radii for heavy elements based on literature reports.

element	radius, Å
Th	1.874 <sup>[25]</sup>
U	1.840 <sup>[25]</sup>
Pu	1.800 <sup>[25]</sup>

*Density Functional Theory Results.* To clarify the results, we present the binding energies with various corrections calculated under both the EtOH and DMF implicit solvation models. From left to right, the columns represent: (1) the uncorrected binding energy in vacuum at 0 K, (2) the binding energy with thermal correction, and (3) the final Gibbs free energy change, incorporating all corrections as outlined in Equation 1.

**Table S6.** Binding energies with various corrections under implicit solvation model (units in kJ/mol).

<b>complex</b>	$\Delta E_{0\text{ K},gas}$	$\Delta E_{298.15\text{ K},gas}$	$\Delta E_{298.15\text{ K},liquid\text{ (EtOH)}}$	$\Delta E_{298.15\text{ K},liquid\text{ (DMF)}}$
MC+ThCl <sub>4</sub>	-188.8	-131.5	-108.6	-106.4
MC+UO <sub>2</sub> Cl <sub>2</sub>	-204.6	-147.7	-50.4	-77.1
MC+PuCl <sub>4</sub>	-186.3	-122.3	-130.1	-131.8

The binding energies of heavy elements, such as ThCl<sub>4</sub> and PuCl<sub>4</sub>, show relatively small differences between the two solvents, with Gibbs free energies remaining consistently negative across both solvation models. This suggests that both solvents provide similar stabilization for these complexes. However, UO<sub>2</sub>Cl<sub>2</sub> exhibits a notably less negative Gibbs free energy in DMF (-77.1 kJ/mol) than in EtOH (-50.4 kJ/mol), indicating a stronger interaction with DMF.

The variability in Gibbs free energies across different metal chlorides and solvents underscores the importance of considering both the metal center and solvent environment when evaluating the stability of these complexes.

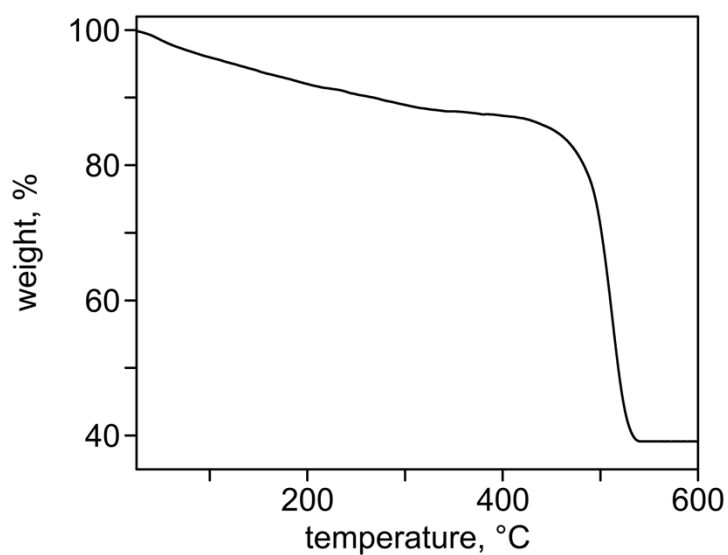


**Figure S2.** TGA plot of UiO-67. The number of defects per metal node was calculated using a reported TGA-based procedure, resulting in an average of four defects per node.<sup>[3]</sup>

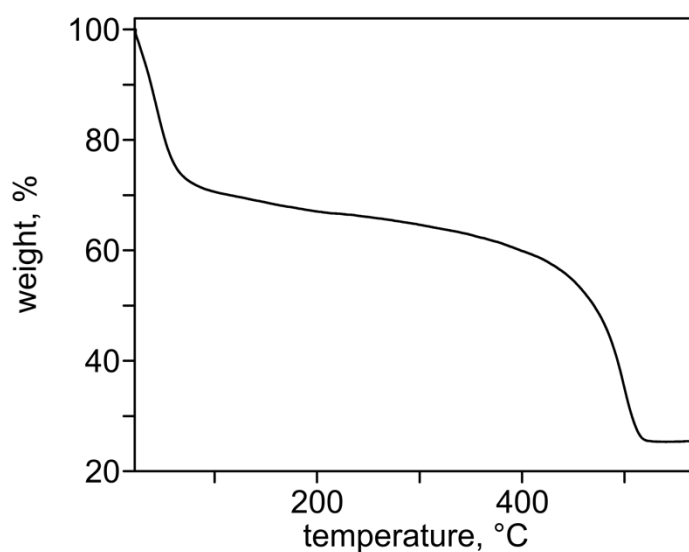


**Figure S3.** TGA plot of UiO-67+SP-COOH. The weight loss before 150 °C corresponds to residual solvent acquired during the thorough washing procedure to remove unbound SP-COOH molecules.

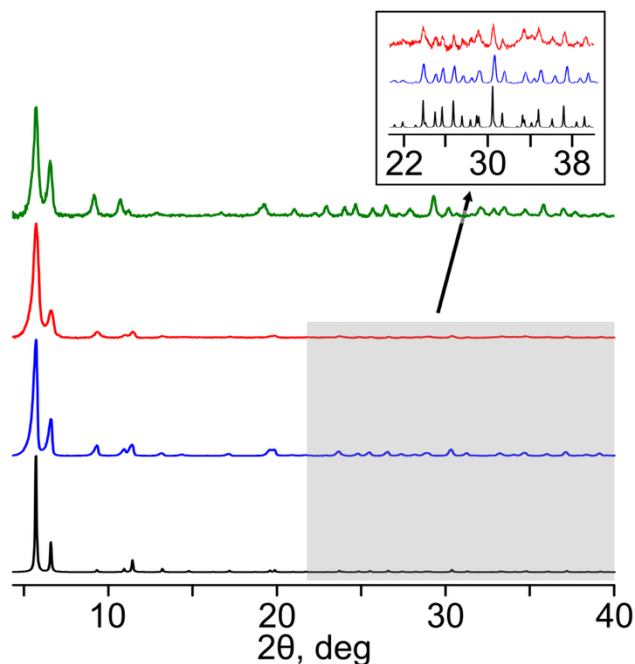


**Figure S4.** PXRD patterns of: simulated UiO-67 (black),<sup>[26]</sup> as-synthesized UiO-67 (blue), UiO-67 after installation of SP-COOH (red), and UiO-67+SP-COOH after actinide capture/release experiments (green). The inset shows the high angle reflections of UiO-67: simulated (black), as-synthesized (blue), and after SP-COOH installation (red).

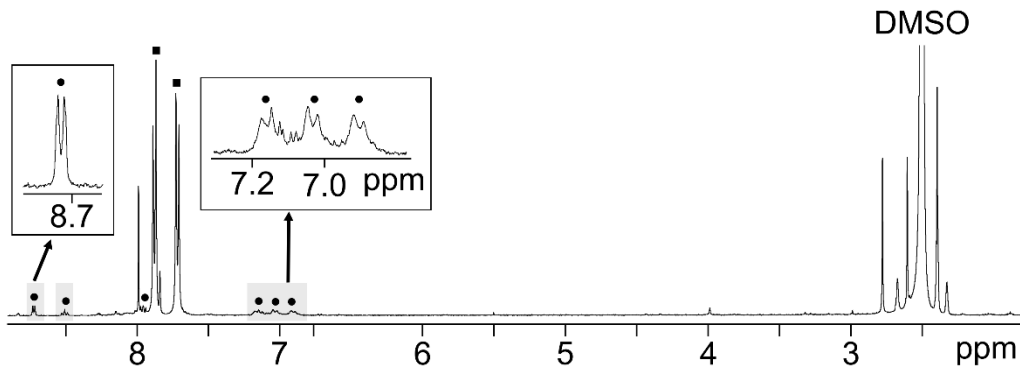


**Figure S5.** <sup>1</sup>H NMR spectrum of digested UiO-67+SP-COOH. The circles indicate resonances corresponding to integrated SP-COOH, and the squares indicate resonances corresponding to the linker of UiO-67.

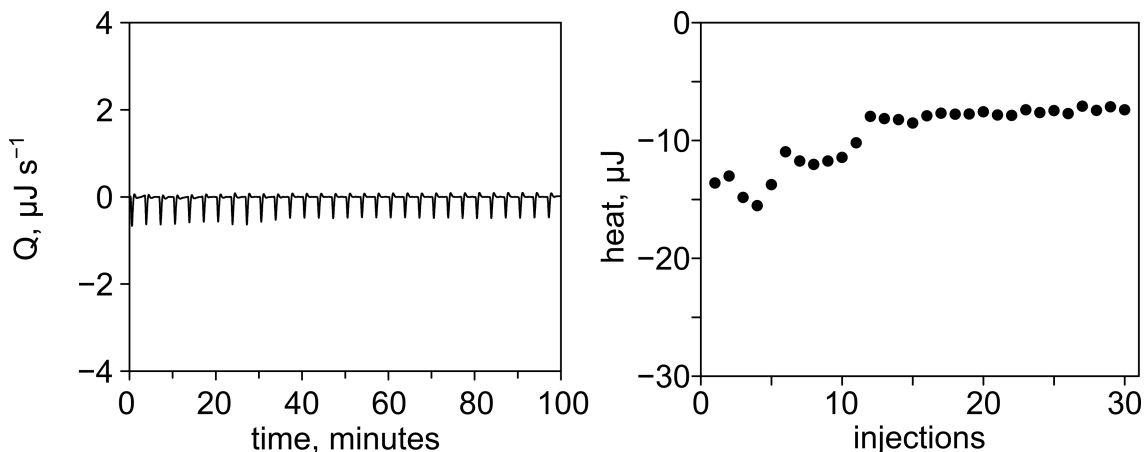


**Figure S6.** ITC thermogram resulting from titration of EtOH (350  $\mu\text{L}$ ) with a  $\text{ThCl}_4$  solution (0.25 mM, 2.5  $\mu\text{L}$  injection in EtOH) as a control experiment.

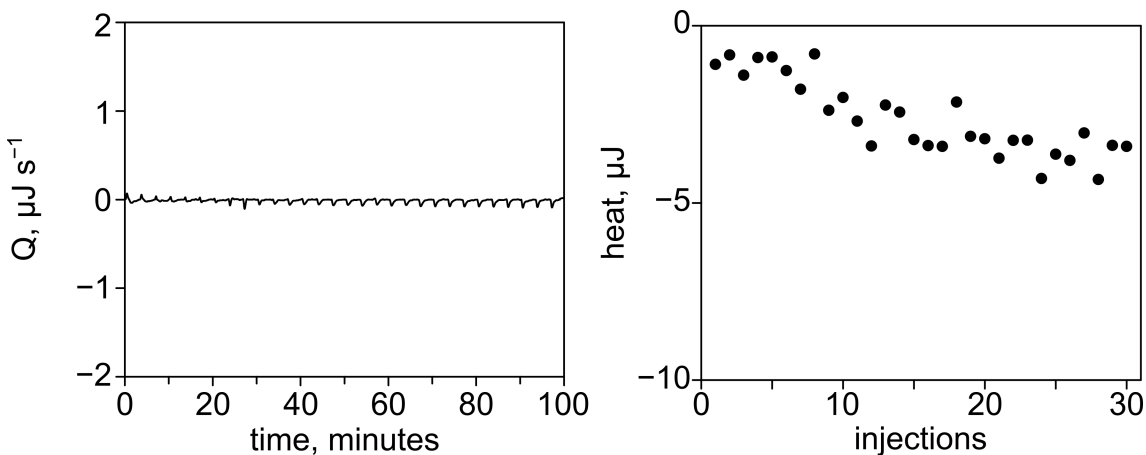


**Figure S7.** ITC thermogram resulting from titration of EtOH (350  $\mu\text{L}$ ) with a  $\text{UCl}_4$  solution (0.25 mM, 2.5  $\mu\text{L}$  injection in EtOH) as a control experiment.

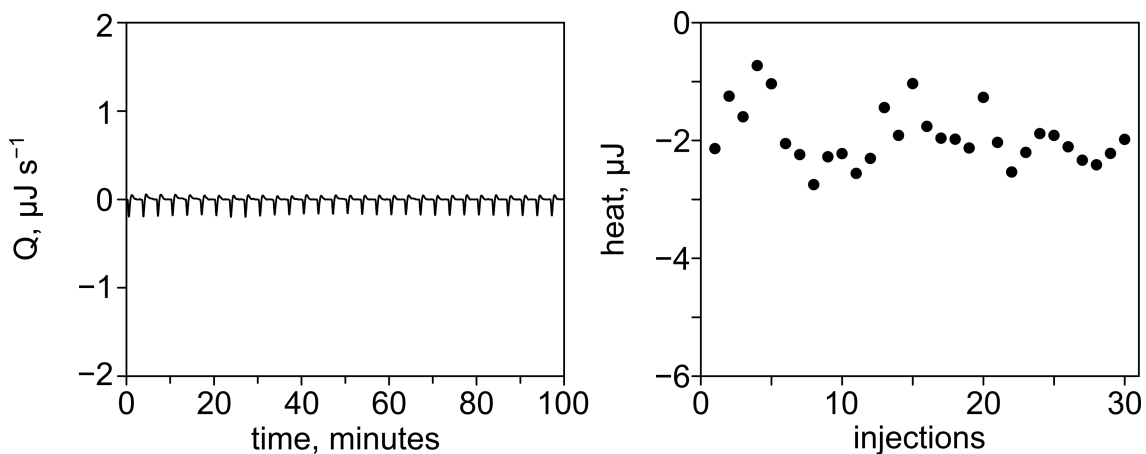


**Figure S8.** ITC thermogram resulting from titration of an MC solution (1 mM, 350  $\mu\text{L}$ ) with EtOH (2.5  $\mu\text{L}$  injection) as a control experiment.

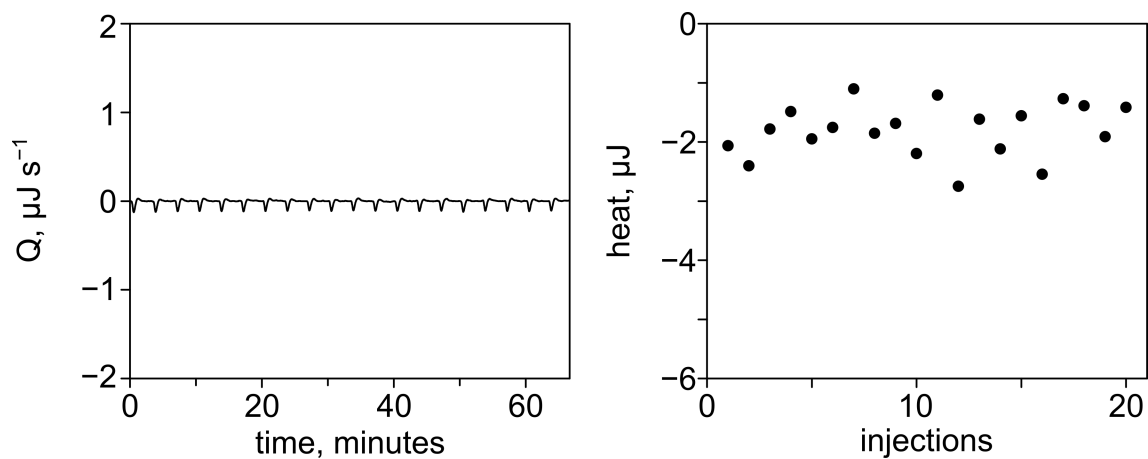


**Figure S9.** ITC thermogram resulting from titration of EtOH (350  $\mu\text{L}$ ) with EtOH (2.5  $\mu\text{L}$  injection) as a control experiment.

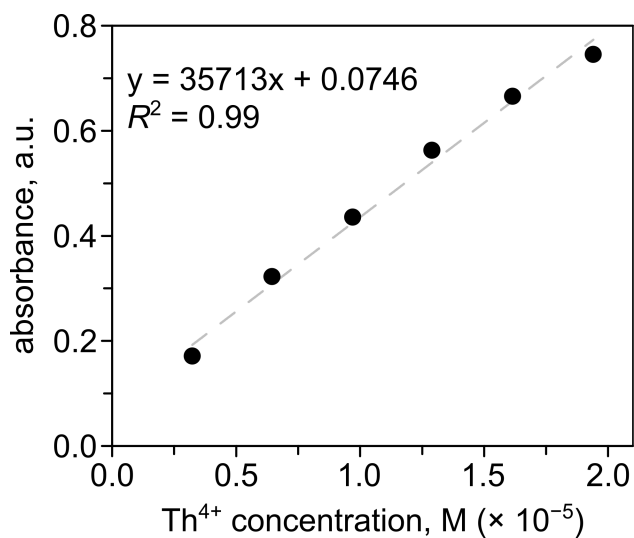


**Figure S10.** Calibration curve used for spectrophotometric determination of thorium cations in the supernatant solution during capture and release experiments. The absorbance of each solution was measured at 667 nm.

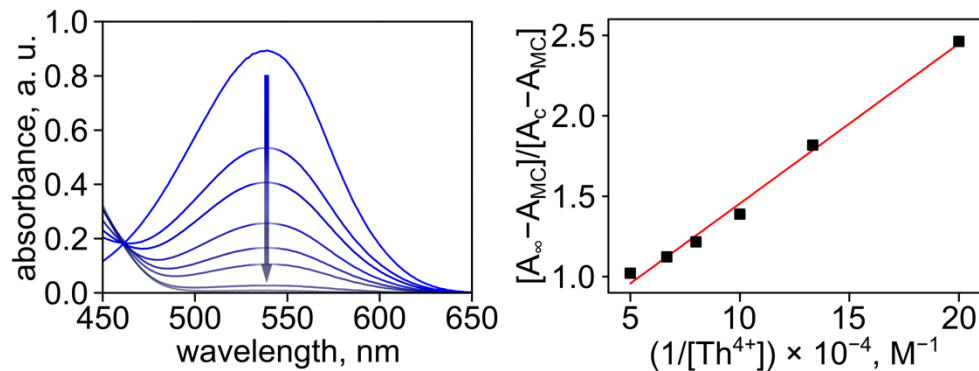


**Figure S11.** (*left*) Absorbance spectra of MC ( $5.0 \times 10^{-5}$  M in EtOH) upon exposure to a 365-nm excitation wavelength for 180 s followed by the addition of 0.00, 0.10, 0.15, 0.20, 0.25, 0.30, 0.40, and 0.50 equiv of ThCl<sub>4</sub> (from top to bottom). (*right*) Plot demonstrating the ratio  $[A_{\infty} - A_{MC}] / [A_C - A_{MC}]$  as a function of  $1/[Th^{4+}]$  for binding constant determination of MC ( $5.0 \times 10^{-5}$  M in EtOH) toward Th<sup>4+</sup>, measured through absorbance changes at 539 nm upon addition of ThCl<sub>4</sub> ( $K_a = 8.8 \pm 3.4 \times 10^4 M^{-1}$ ,  $R^2 = 0.99$ ).

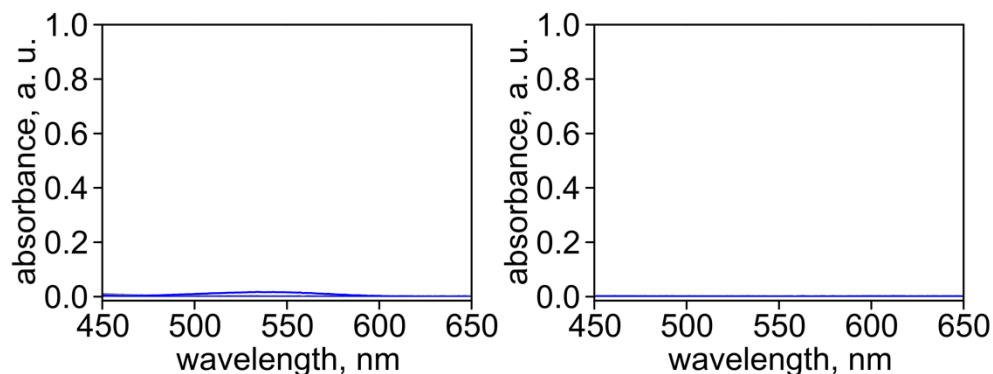


**Figure S12.** Control experiments performed to evaluate possible interactions between SP and ThCl<sub>4</sub> in EtOH in the dark. (*left*) Absorbance spectra of SP ( $5.0 \times 10^{-5}$  M in EtOH) in the dark followed by the addition of 0.00, 0.10, 0.15, 0.20, 0.25, 0.30, 0.40, and 0.50 equiv of ThCl<sub>4</sub>. (*right*) Absorbance spectra of  $5.00 \times 10^{-6}$ ,  $7.50 \times 10^{-6}$ ,  $1.00 \times 10^{-5}$ ,  $1.25 \times 10^{-5}$ ,  $1.50 \times 10^{-5}$ ,  $2.00 \times 10^{-5}$ , and  $2.50 \times 10^{-5}$  M of ThCl<sub>4</sub> in EtOH.

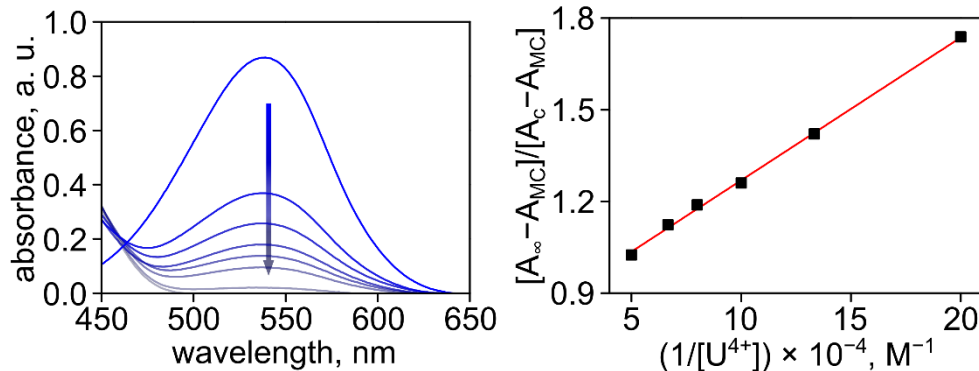


**Figure S13.** (left) Absorbance spectra of MC ( $5.0 \times 10^{-5}$  M in EtOH) upon exposure to a 365-nm excitation wavelength for 180 s followed by the addition of 0.00, 0.10, 0.15, 0.25, 0.30, 0.40, and 1.00 equivalents of  $UCl_4$  (from top to bottom). (right) Plot demonstrating the ratio  $[A_{\infty} - A_{MC}] / [A_C - A_{MC}]$  as a function of  $1/[U^{4+}]$  for binding constant determination of MC ( $2.5 \times 10^{-5}$  M in EtOH) toward  $U^{4+}$ , measured through absorbance changes at 539 nm upon addition of  $UCl_4$  ( $K_a = 1.3 \pm 0.5 \times 10^5 M^{-1}$ ,  $R^2 = 0.99$ ).

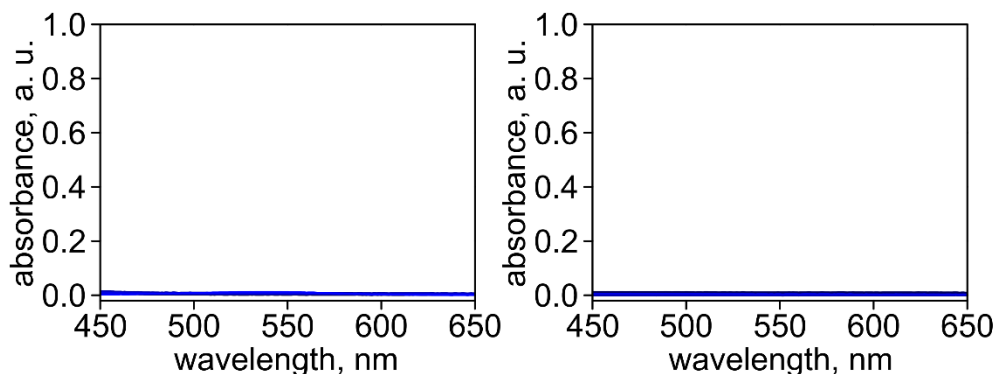


**Figure S14.** Control experiments performed to evaluate possible interactions between SP and  $UCl_4$  in EtOH in the dark. (left) Absorbance spectra of SP ( $5.0 \times 10^{-5}$  M in EtOH) without irradiation followed by the addition of 0.00, 0.10, 0.15, 0.20, 0.25, 0.30, 0.40, and 1.00 equivalents of  $UCl_4$ . (right) Absorbance spectra of  $5.00 \times 10^{-6}$ ,  $7.50 \times 10^{-6}$ ,  $1.00 \times 10^{-5}$ ,  $1.25 \times 10^{-5}$ ,  $1.50 \times 10^{-5}$ ,  $2.00 \times 10^{-5}$ ,  $5.00 \times 10^{-5}$  M of  $UCl_4$  in EtOH.

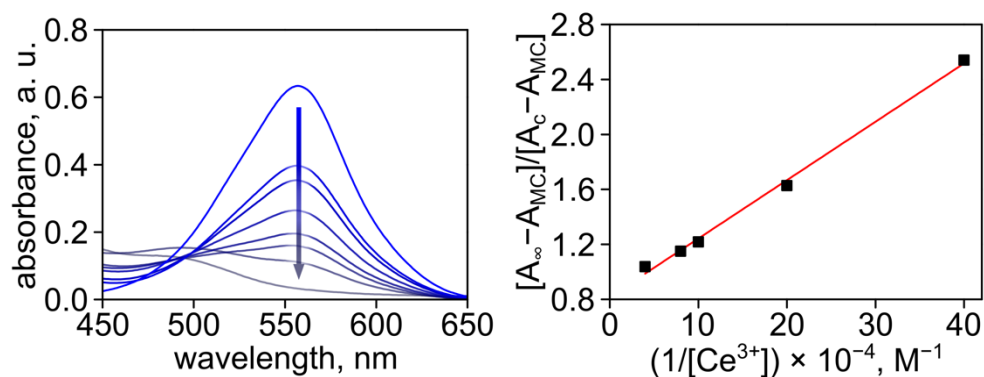


**Figure S15.** (*left*) Absorbance spectra of MC ( $2.5 \times 10^{-5}$  M in MeCN) upon exposure to a 365-nm excitation wavelength for 180 s followed by the addition of 0.00, 0.10, 0.15, 0.20, 0.25, 0.30, 1.0, and 2.0 equivalents of Ce(NO<sub>3</sub>)<sub>3</sub> (from top to bottom). (*right*) Plot demonstrating the ratio  $[A_{\infty} - A_{MC}] / [A_C - A_{MC}]$  as a function of  $1/[Ce^{3+}]$  for binding constant determination of MC ( $2.5 \times 10^{-5}$  M in MeCN) toward Ce<sup>3+</sup>, measured through absorbance changes at 557 nm upon addition of Ce(NO<sub>3</sub>)<sub>3</sub> ( $K_a = 2.3 \pm 1.2 \times 10^5 M^{-1}$ ,  $R^2 = 0.99$ ).

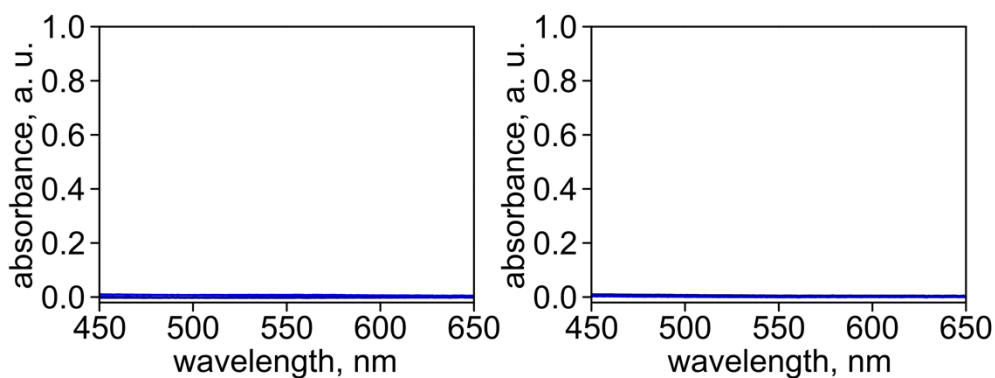


**Figure S16.** Control experiments performed to evaluate possible interactions between SP and Ce(NO<sub>3</sub>)<sub>3</sub> in MeCN in the dark. (*left*) Absorbance spectra of SP ( $2.5 \times 10^{-5}$  M in MeCN) without irradiation followed by the addition of 0.00, 0.10, 0.15, 0.20, 0.25, 0.30, 1.0, and 2.0 equivalents of Ce(NO<sub>3</sub>)<sub>3</sub>. (*right*) Absorbance spectra of  $2.50 \times 10^{-6}$ ,  $3.75 \times 10^{-6}$ ,  $5.00 \times 10^{-6}$ ,  $6.25 \times 10^{-6}$ ,  $7.50 \times 10^{-6}$ ,  $2.50 \times 10^{-5}$ , and  $5.00 \times 10^{-5}$  M of Ce(NO<sub>3</sub>)<sub>3</sub> in MeCN.

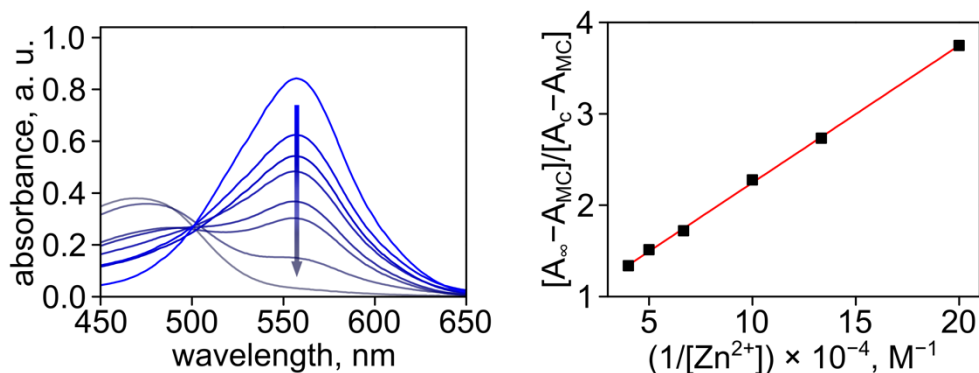


**Figure S17.** (*left*) Absorbance spectra of MC ( $2.5 \times 10^{-5}$  M in MeCN) upon exposure to a 365-nm excitation wavelength for 180 s followed by the addition of 0.00, 0.20, 0.30, 0.40, 0.60, 0.80, 2.0, and 10 equiv of ZnI<sub>2</sub> (from top to bottom). (*right*) Plot demonstrating the ratio  $[A_{\infty} - A_{MC}] / [A_c - A_{MC}]$  as a function of  $1/[Zn^{2+}]$  for binding constant determination of MC ( $2.5 \times 10^{-5}$  M in MeCN) toward Zn<sup>2+</sup>, measured through absorbance changes at 557 nm upon addition of ZnI<sub>2</sub> ( $K_a = 6.5 \pm 0.5 \times 10^4 M^{-1}$ ,  $R^2 = 0.99$ ).

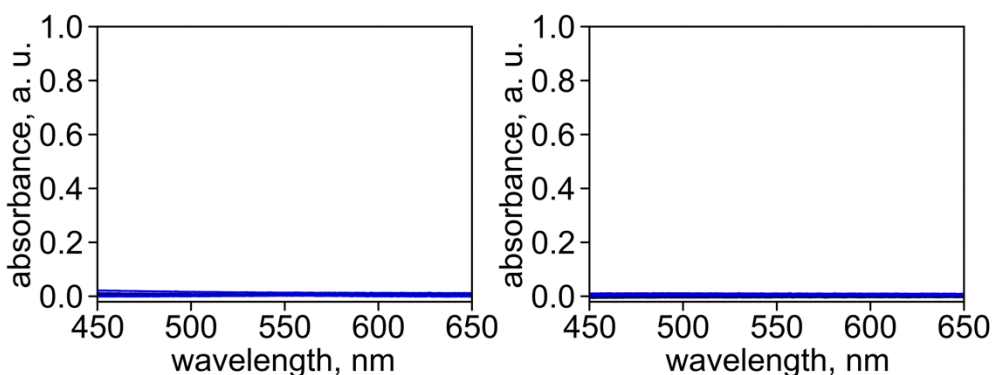


**Figure S18.** Control experiment performed to evaluate possible interactions between SP and ZnI<sub>2</sub> in MeCN in the dark. (*left*) Absorbance spectra of SP ( $2.5 \times 10^{-5}$  M in MeCN) without irradiation followed by the addition of 0.00, 0.20, 0.30, 0.40, 0.60, 0.80, 2.0, and 10 equiv of ZnI<sub>2</sub>. (*right*) Absorbance spectra of  $5.00 \times 10^{-6}$ ,  $7.50 \times 10^{-6}$ ,  $1.00 \times 10^{-5}$ ,  $1.50 \times 10^{-5}$ ,  $2.00 \times 10^{-5}$ ,  $5.00 \times 10^{-5}$ ,  $5.00 \times 10^{-4}$  M of ZnI<sub>2</sub> in MeCN.

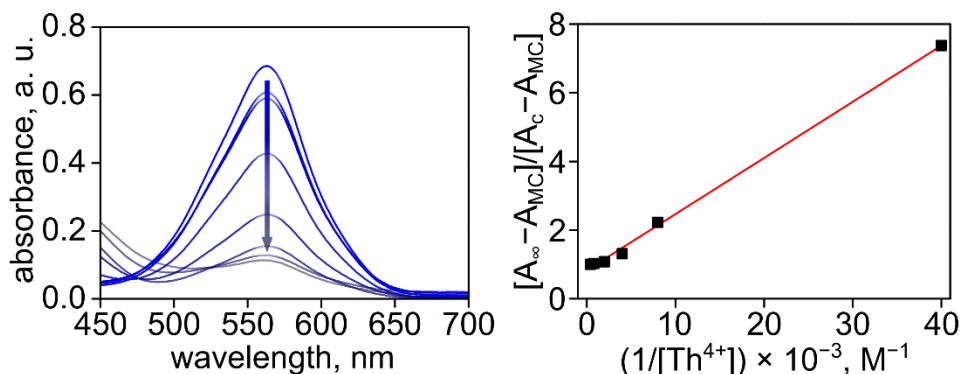


**Figure S19.** (*left*) Absorbance spectra of MC ( $2.5 \times 10^{-5}$  M in DMF) upon exposure to a 365-nm excitation wavelength for 180 s followed by the addition of 0.0, 1.0, .2.0, 5.0, 10, 20, 50, and 100 equivalents of ThCl<sub>4</sub> (from top to bottom). (*right*) Plot demonstrating the ratio  $[A_{\infty} - A_{MC}] / [A_C - A_{MC}]$  as a function of  $1/[Th^{4+}]$  for binding constant determination of MC ( $2.5 \times 10^{-5}$  M in DMF) toward Th<sup>4+</sup>, measured through absorbance changes at 565 nm upon addition of ThCl<sub>4</sub> ( $K_a = 7.3 \pm 0.8 \times 10^3 \text{ M}^{-1}$ ,  $R^2 = 0.99$ ).

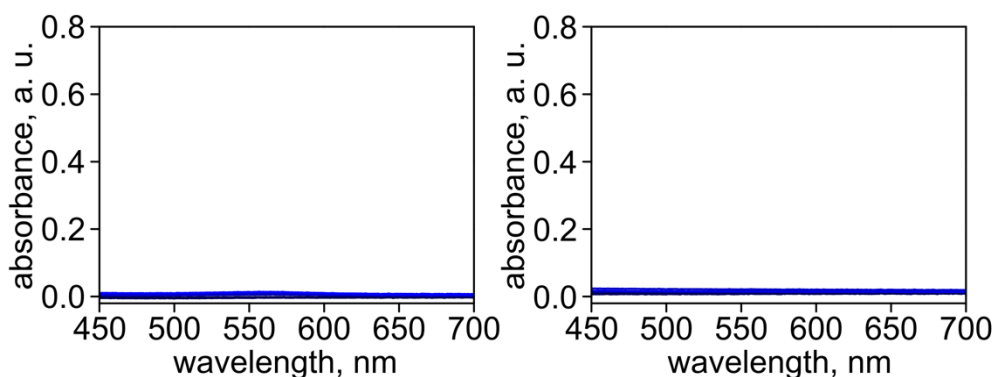


**Figure S20.** Control experiments performed to evaluate possible interactions between SP and ThCl<sub>4</sub> in DMF in the dark. (*left*) Absorbance spectra of SP ( $2.5 \times 10^{-5}$  M in DMF) without irradiation followed by the addition of 0.0, 1.0, .2.0, 5.0, 10, 20, 50, and 100 equivalents of ThCl<sub>4</sub>. (*right*) Absorbance spectra of  $2.50 \times 10^{-5}$ ,  $5.00 \times 10^{-5}$ ,  $1.25 \times 10^{-4}$ ,  $2.50 \times 10^{-4}$ ,  $2.50 \times 10^{-4}$ ,  $1.25 \times 10^{-3}$ , and  $2.50 \times 10^{-3}$  M of ThCl<sub>4</sub> in DMF.

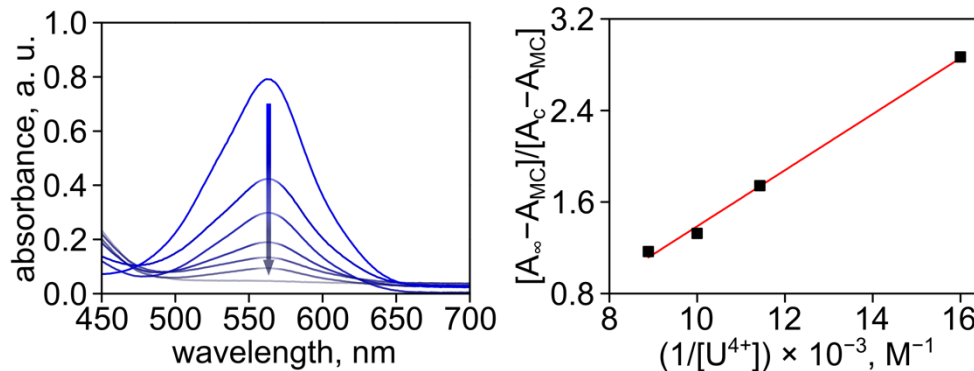


**Figure S21.** (left) Absorbance spectra of MC ( $2.5 \times 10^{-5}$  M in DMF) upon exposure to a 365-nm excitation wavelength for 180 s followed by the addition of 0.00, 3.0, 3.5, 4.0, 4.5, 5.0, and 20 equivalents of  $UCl_4$  (from top to bottom). (right) Plot demonstrating the ratio  $[A_{\infty} - A_{MC}] / [A_C - A_{MC}]$  as a function of  $1/[U^{4+}]$  for binding constant determination of MC ( $2.5 \times 10^{-5}$  M in DMF) toward  $U^{4+}$ , measured through absorbance changes at 565 nm addition of  $UCl_4$  ( $K_a = 5.8 \pm 0.6 \times 10^3 M^{-1}$ ,  $R^2 = 0.99$ ).

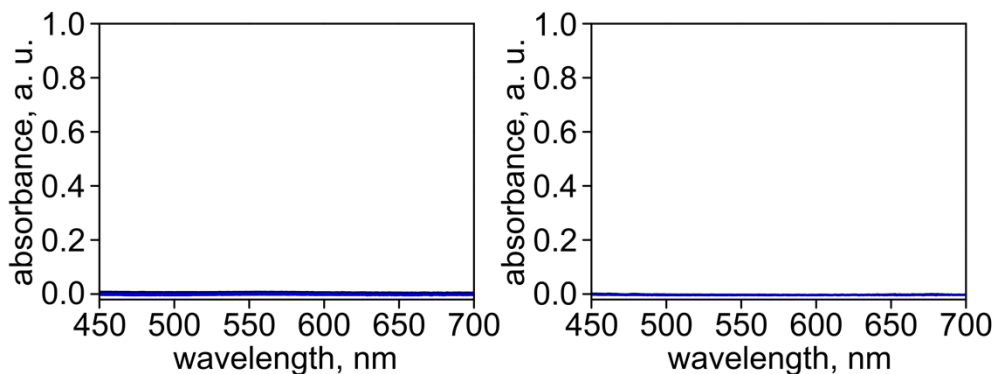


**Figure S22.** Control experiments performed to evaluate possible interactions between SP and  $UCl_4$  in DMF in the dark. (left) Absorbance spectra of SP ( $2.5 \times 10^{-5}$  M in DMF) without irradiation followed by the addition of 0.00, 3.0, 3.5, 4.0, 4.5, 5.0, and 20 equiv of  $UCl_4$ . (right) Absorbance spectra of  $7.50 \times 10^{-5}$ ,  $8.75 \times 10^{-5}$ ,  $1.00 \times 10^{-4}$ ,  $1.13 \times 10^{-4}$ ,  $1.25 \times 10^{-4}$ , and  $5.00 \times 10^{-4}$  M of  $UCl_4$  in DMF.

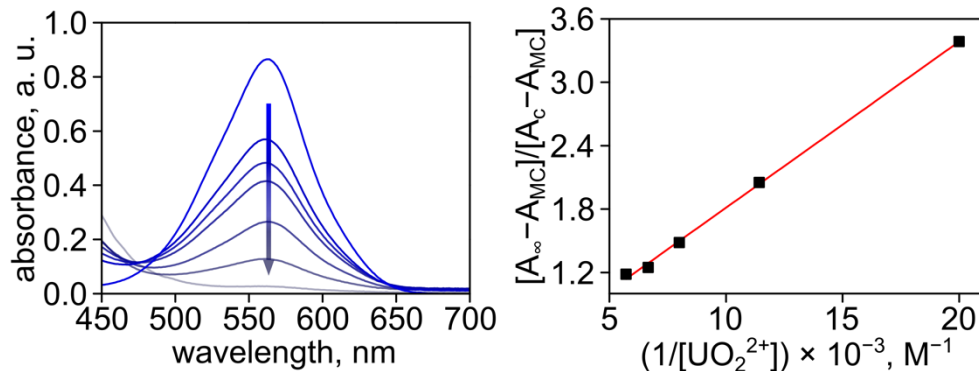


**Figure S23.** (left) Absorbance spectra of MC ( $2.5 \times 10^{-5}$  M in DMF) upon exposure to a 365-nm excitation wavelength for 180 s followed by the addition of 0.00, 3.0, 3.5, 4.0, 4.5, 7.5, and 50 equivalents of  $UO_2(NO_3)_2$  (from top to bottom). (right) Plot demonstrating the ratio  $[A_{\infty} - A_{MC}] / [A_C - A_{MC}]$  as a function of  $1/[UO_2^{2+}]$  for binding constant determination of MC ( $2.5 \times 10^{-5}$  M in DMF) toward  $UO_2^{2+}$ , measured through absorbance changes at 565 nm upon addition of  $UO_2(NO_3)_2$  ( $K_a = 5.3 \pm 1.1 \times 10^3 M^{-1}$ ,  $R^2 = 0.99$ ).

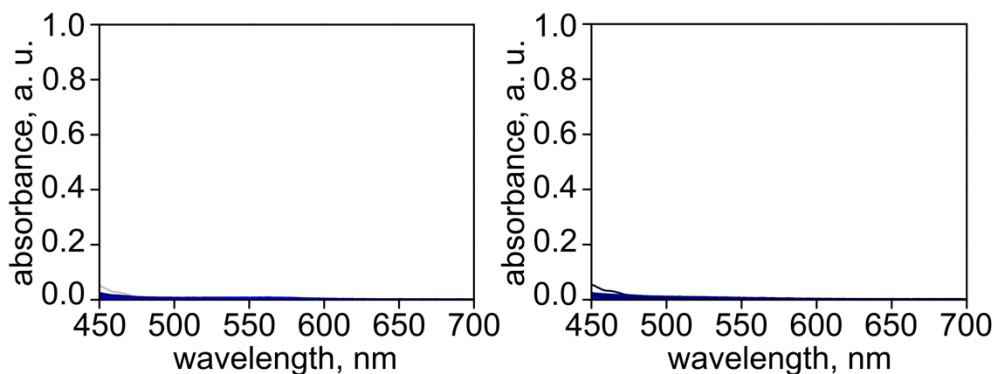


**Figure S24.** Control experiments performed to evaluate possible interactions between SP and  $UO_2(NO_3)_2$  in DMF in the dark. (left) Absorbance spectra of SP ( $2.5 \times 10^{-5}$  M in DMF) without irradiation followed by the addition of 0.00, 3.0, 3.5, 4.0, 4.5, 7.5, and 50 equiv of  $UO_2(NO_3)_2$ . (right) Absorbance spectra of  $7.50 \times 10^{-5}$ ,  $8.75 \times 10^{-5}$ ,  $1.00 \times 10^{-4}$ ,  $1.13 \times 10^{-4}$ ,  $1.88 \times 10^{-4}$ , and  $1.25 \times 10^{-3}$  M of  $UO_2(NO_3)_2$  in DMF.

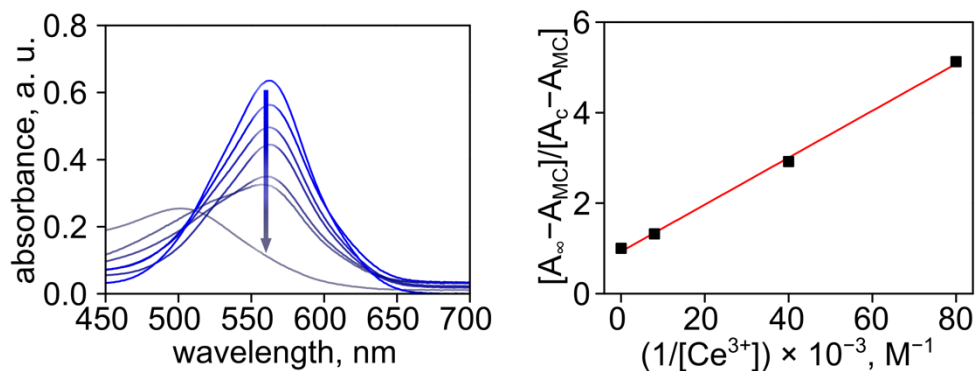


**Figure S25.** (left) Absorbance spectra of MC ( $2.5 \times 10^{-5}$  M in DMF) upon exposure to a 365-nm excitation wavelength for 180 s followed by the addition of 0, 1, 5, 10, 100, 500, 1000, and 10000 equiv of  $\text{Ce}(\text{NO}_3)_3$  (from top to bottom). (right) Plot demonstrating the ratio  $[A_\infty - A_{\text{MC}}]/[A_{\text{C}} - A_{\text{MC}}]$  as a function of  $1/[\text{Ce}^{3+}]$  for binding constant determination of MC ( $2.5 \times 10^{-5}$  M in DMF) toward  $\text{Ce}^{3+}$ , measured through absorbance changes at 565 nm upon addition of  $\text{Ce}(\text{NO}_3)_3$  ( $K_a = 2.1 \pm 0.6 \times 10^4 \text{ M}^{-1}$ ,  $R^2 = 0.99$ ).

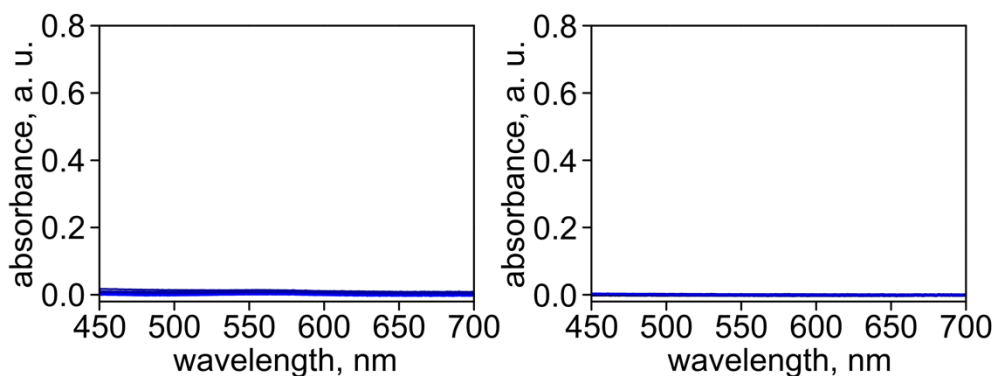


**Figure S26.** Control experiment performed to evaluate possible interactions between SP and  $\text{Ce}(\text{NO}_3)_3$  in DMF in the dark. (left) Absorbance spectra of SP ( $2.5 \times 10^{-5}$  M in DMF) without irradiation followed by the addition of 0, 1, 5, 10, 100, 500, 1000, and 10000 equivalents of  $\text{Ce}(\text{NO}_3)_3$ . (right) Absorbance spectra of  $2.50 \times 10^{-5}$ ,  $1.25 \times 10^{-4}$ ,  $2.50 \times 10^{-4}$ ,  $2.50 \times 10^{-3}$ ,  $1.25 \times 10^{-2}$ ,  $2.50 \times 10^{-2}$ , and  $2.50 \times 10^{-1}$  M of  $\text{Ce}(\text{NO}_3)_3$  in DMF.

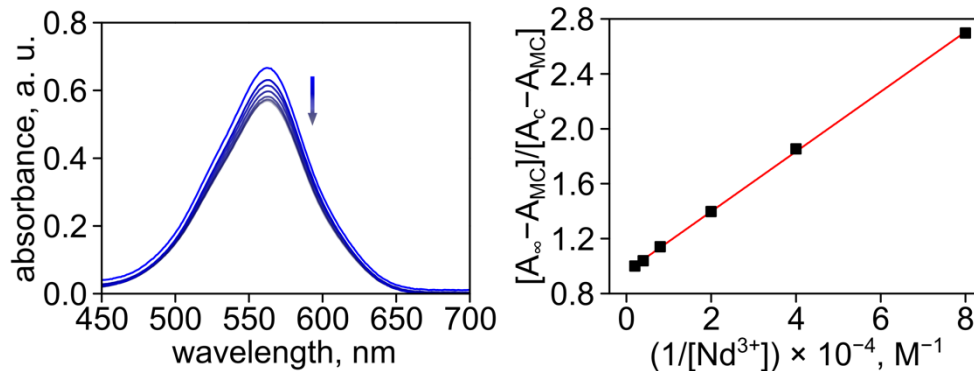


**Figure S27.** (left) Absorbance spectra of MC ( $2.5 \times 10^{-5}$  M in DMF) upon exposure to a 365-nm excitation wavelength for 180 s followed by the addition of 0.00, 0.50, 1.0, 2.0, 5.0, 10, and 20 equivalents of  $NdCl_3$  (from top to bottom). (right) Plot demonstrating the ratio  $[A_{\infty} - A_{MC}] / [A_C - A_{MC}]$  as a function of  $1/[Nd^{3+}]$  for binding constant determination of MC ( $2.5 \times 10^{-5}$  M in DMF) toward  $Nd^{3+}$ , measured through absorbance changes at 565 nm upon addition of  $NdCl_3$  ( $K_a = 5.2 \pm 0.5 \times 10^4 M^{-1}$ ,  $R^2 = 0.99$ ).

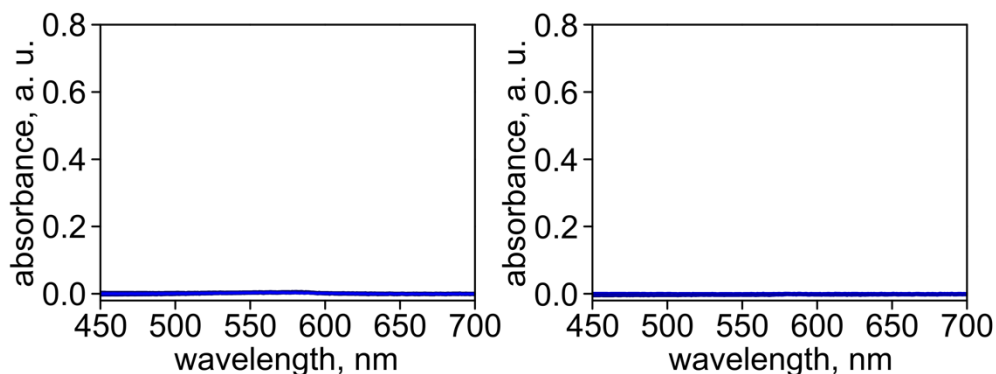


**Figure S28.** Control experiments performed to evaluate possible interactions between SP and  $NdCl_3$  in DMF in the dark. (left) Absorbance spectra of SP ( $2.5 \times 10^{-5}$  M in DMF) without irradiation followed by the addition of 0.00, 0.50, 1.0, 2.0, 5.0, 10, and 20 equivalents of  $NdCl_3$ . (right) Absorbance spectra of  $1.25 \times 10^{-5}$ ,  $2.50 \times 10^{-5}$ ,  $5.00 \times 10^{-5}$ ,  $1.25 \times 10^{-4}$ ,  $2.50 \times 10^{-4}$ , and  $5.00 \times 10^{-4}$  M of  $NdCl_3$  in DMF.

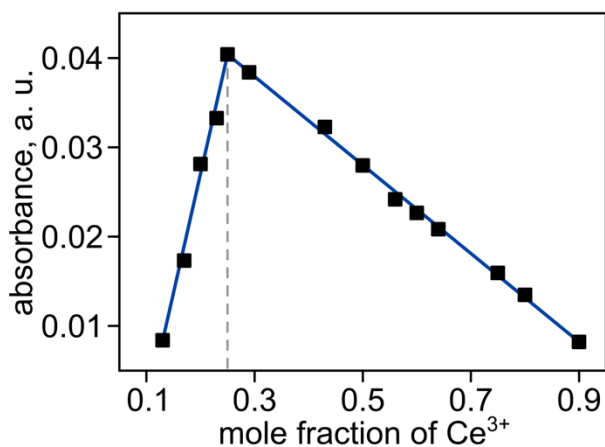


**Figure S29.** Job's plot demonstrating the relationship between the mole fraction of Ce(NO<sub>3</sub>)<sub>3</sub> and absorbance at 433 nm, corresponding to the formation of an MC–Ce<sup>3+</sup> metal complex in DMF. The determined complex stoichiometry was 3:1 (MC : Ce<sup>3+</sup>).

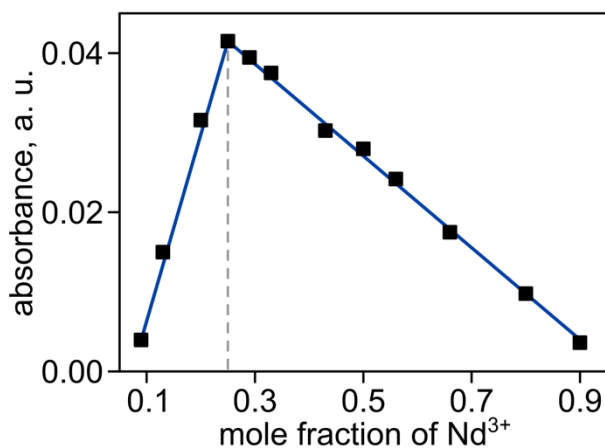


**Figure S30.** Job's plot demonstrating the relationship between the mole fraction of NdCl<sub>3</sub> and absorbance at 433 nm, corresponding to the formation of an MC–Nd<sup>3+</sup> metal complex in DMF. The determined complex stoichiometry was 3:1 (MC : Nd<sup>3+</sup>).

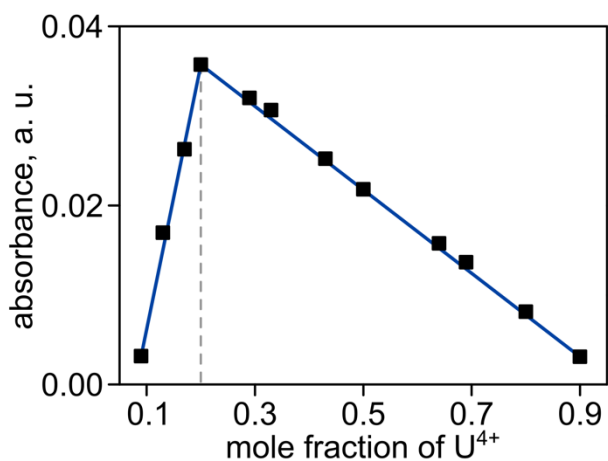


**Figure S31.** Job's plot demonstrating the relationship between the mole fraction of  $UCl_4$  and absorbance at 433 nm, corresponding to the formation of an  $MC-U^{4+}$  metal complex in DMF. The determined complex stoichiometry was 4:1 (MC :  $U^{4+}$ ).

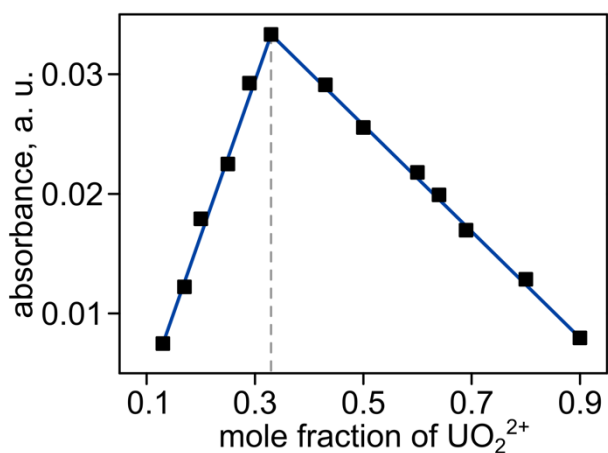


**Figure S32.** Job's plot demonstrating the relationship between the mole fraction of  $UO_2(NO_3)_2$  and absorbance at 433 nm, corresponding to the formation of an  $MC-UO_2^{2+}$  metal complex in DMF. The determined complex stoichiometry was 2:1 (MC :  $UO_2^{2+}$ ).

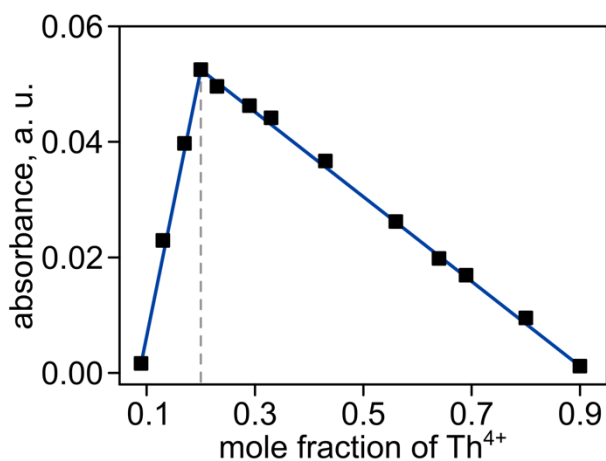


**Figure S33.** Job's plot demonstrating the relationship between the mole fraction of ThCl<sub>4</sub> and absorbance at 433 nm, corresponding to the formation of an MC–Th<sup>4+</sup> metal complex in DMF. The determined complex stoichiometry was 4:1 (MC : Th<sup>4+</sup>).

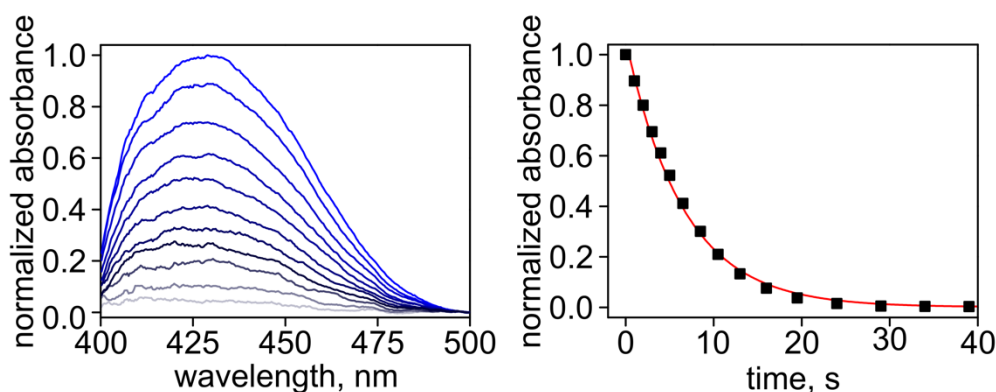


**Figure S34.** (left) Normalized UV-vis absorbance spectra of SP+ThCl<sub>4</sub> (1:1 molar ratio, 3 mM in EtOH) upon exposure to 365-nm irradiated for 30 s followed by attenuation under visible light ( $\lambda_{\text{ex}} = 400\text{--}900\text{ nm}$ ). (right) Kinetic studies of SP+ThCl<sub>4</sub> (1:1 molar ratio, 3 mM in EtOH) showing a decrease in absorbance upon exposure to visible light ( $k = 0.16\text{ s}^{-1}$ ,  $R^2 = 0.99$ ).

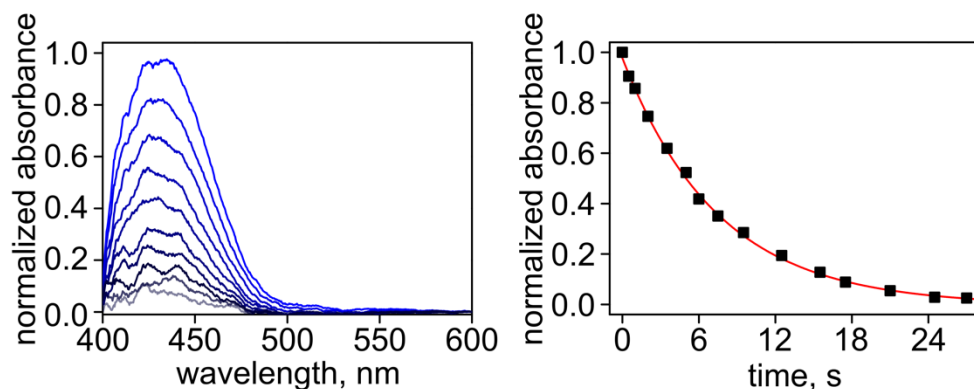


**Figure S35.** (*left*) Normalized UV-vis absorbance spectra of SP+UCl<sub>4</sub> (1:1 molar ratio, 3 mM in EtOH) upon exposure to 365-nm irradiated for 30 s followed by attenuation under visible light ( $\lambda_{\text{ex}} = 400\text{--}900$  nm). (*right*) Kinetic studies of SP+UCl<sub>4</sub> (1:1 molar ratio, 3 mM in EtOH) showing a decrease in absorbance upon exposure to visible light ( $k = 0.13$  s<sup>-1</sup>,  $R^2 = 0.99$ ).

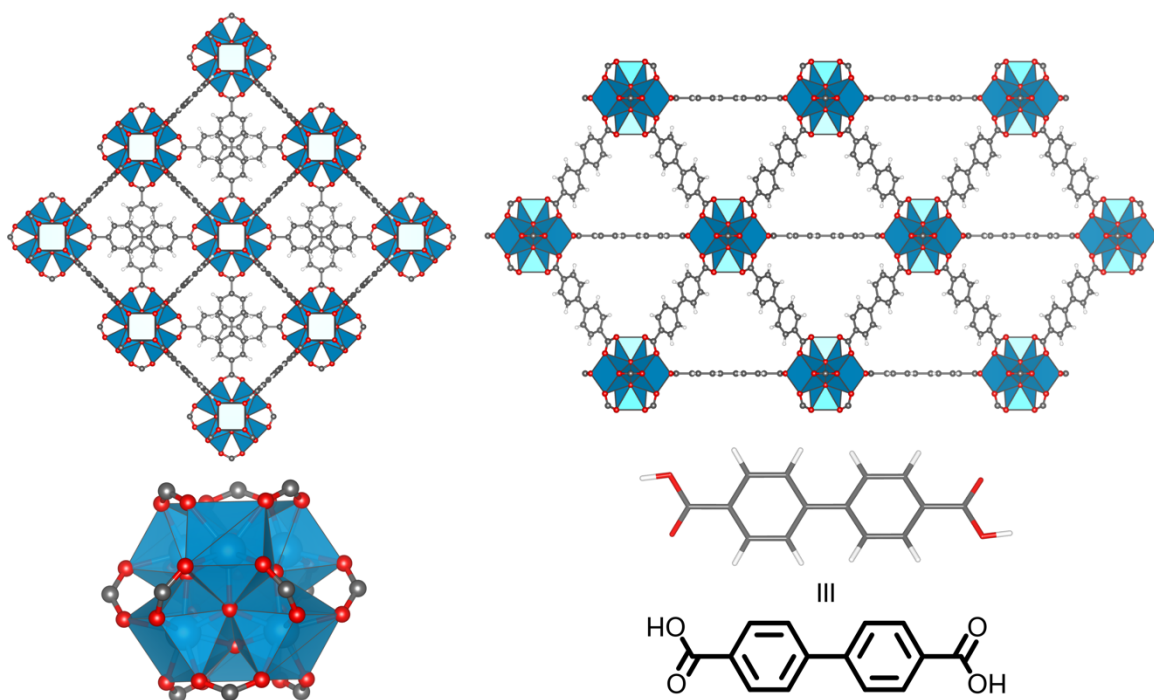


**Figure S36.** (*top*) Two views of the single crystal X-ray structure of UiO-67.<sup>[28]</sup> (*bottom*) The metal node of UiO-67 and the structure of the organic linker, 4,4'-biphenyldicarboxylic acid (H<sub>2</sub>BPDC), used for MOF preparation. The blue polyhedra represent zirconium atoms, and the red, gray, and white spheres represent oxygen, carbon, and hydrogen atoms, respectively.

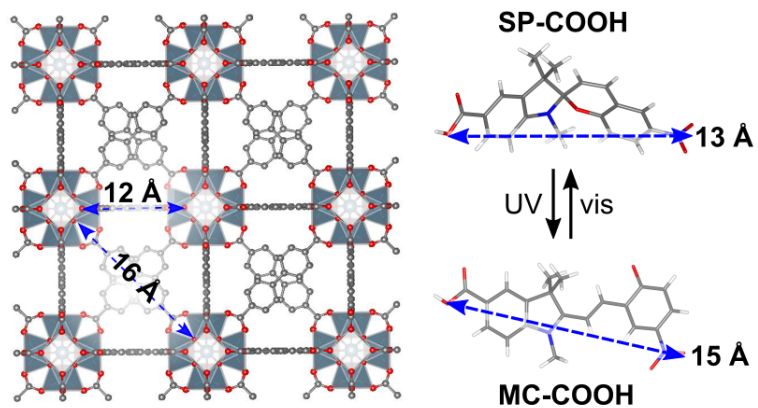


**Figure S37.** X-ray crystal structures of UiO-67 (*left*) and both isomers of SP-COOH (*right*). The pore dimensions of UiO-67 and the molecular length of SP-COOH and MC-COOH are highlighted.

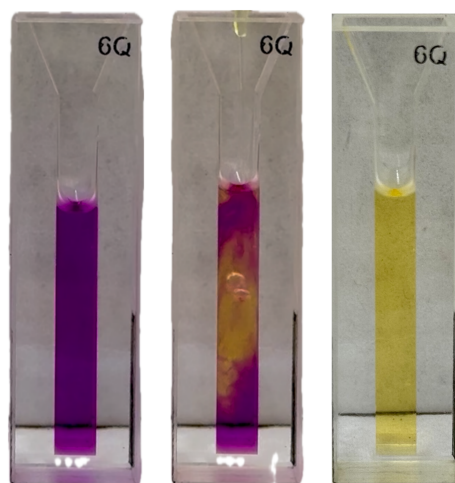


**Figure S38.** Photographs of a 10 mM MC solution in MeCN (*left*), as well as upon addition of a 10 mM solution of ZnI<sub>2</sub> in MeCN (*middle*), and after mixing the two solutions (*right*).

### X-ray crystal structure refinement for MC-COOH ( $[\text{C}_{20}\text{H}_{19}\text{N}_2\text{O}_5]\text{Cl}$ ).

X-ray intensity data from an orange needle were collected at 100(2) K using a Bruker D8 QUEST diffractometer equipped with a PHOTON-II area detector and an Incoatec microfocus source (Mo  $K_\alpha$  radiation,  $\lambda = 0.71073 \text{ \AA}$ ). The raw area detector data frames were reduced, scaled and corrected for absorption effects using the Bruker APEX3, SAINT+ and SADABS programs.<sup>[5,6]</sup> The structure was solved with SHELXT.<sup>[7,8]</sup> Subsequent difference Fourier calculations and full-matrix least-squares refinement against  $F^2$  were performed with SHELXL-2018<sup>[7,8]</sup> using OLEX2.<sup>[9]</sup>

The compound crystallizes in the orthorhombic system. The pattern of systematic absences in the intensity data was uniquely consistent with the space group  $Pbca$ , which was confirmed by structure solution. The asymmetric unit consists of one  $\text{C}_{20}\text{H}_{19}\text{N}_2\text{O}_5^+$  cation and one chloride anion. All non-hydrogen atoms were refined with anisotropic displacement parameters. Hydrogen atoms bonded to carbon were located in difference Fourier maps before being placed in geometrically idealized positions and included as riding atoms with  $d(\text{C-H}) = 0.95 \text{ \AA}$  and  $U_{\text{iso}}(\text{H}) = 1.2U_{\text{eq}}(\text{C})$  for arene hydrogen atoms and  $d(\text{C-H}) = 0.98 \text{ \AA}$  and  $U_{\text{iso}}(\text{H}) = 1.5U_{\text{eq}}(\text{C})$  for methyl hydrogens. The methyl hydrogens were allowed to rotate as a rigid group to the orientation of maximum observed electron density. Hydrogen atoms bonded to oxygen were located and refined freely. The largest residual electron density peak in the final difference map is  $0.37 \text{ e}^-/\text{\AA}^3$ , located  $0.95 \text{ \AA}$  from Cl1.

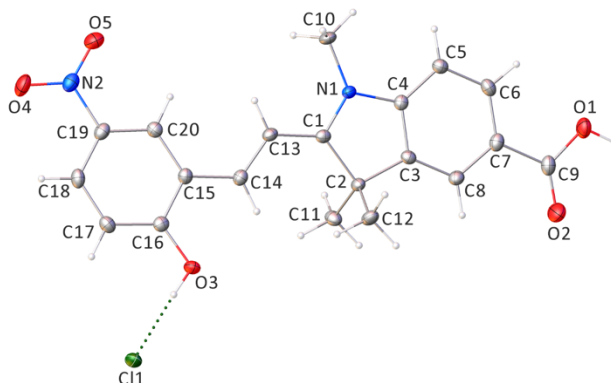


**Figure S39.** X-ray crystal structure of MC-COOH ( $[\text{C}_{20}\text{H}_{19}\text{N}_2\text{O}_5]\text{Cl}$ ). Displacement ellipsoids are drawn at the 50% probability level.

**Table S7.** X-ray structure refinement data for MC-COOH ([C<sub>20</sub>H<sub>19</sub>N<sub>2</sub>O<sub>5</sub>]Cl).

compound	MC-COOH
formula	C <sub>20</sub> H <sub>19</sub> ClN <sub>2</sub> O <sub>5</sub>
FW, g·mol <sup>-1</sup>	402.82
<i>T</i> , K	100(2)
crystal system	orthorhombic
space group	<i>Pbca</i>
<i>Z</i>	8
<i>a</i> , Å	6.8431(3)
<i>b</i> , Å	21.1213(9)
<i>c</i> , Å	26.1977(11)
$\alpha$ , °	90
$\beta$ , °	90
$\gamma$ , °	90
<i>V</i> , Å <sup>3</sup>	3786.5(3)
<i>d</i> <sub>calc</sub> , g cm <sup>-3</sup>	1.413
$\mu$ , mm <sup>-1</sup>	0.237
F(000)	1680.0
crystal size, mm <sup>3</sup>	0.22 × 0.04 × 0.03
2 theta range	3.856 to 55.07
index ranges	-8 ≤ <i>h</i> ≤ 8 -27 ≤ <i>k</i> ≤ 27 -34 ≤ <i>l</i> ≤ 34
reflections collected	53020
data/restraints/parameters	4354/0/264
GOF on <i>F</i> <sup>2</sup>	1.095
largest peak/hole, e/Å <sup>3</sup>	0.37/-0.32
<i>R</i> <sub>1</sub> ( <i>wR</i> <sub>2</sub> ), %, [ <i>I</i> ≥ 2σ( <i>I</i> )] <sup>b</sup>	0.0532 (0.1060)

<sup>a</sup>Mo-K $\alpha$  ( $\lambda = 0.71073$  Å) radiation<sup>b</sup> $R_1 = \sum ||F_o| - |F_c|| / \sum |F_o|$ ,  $wR_2 = -\sum [w(F_o^2 - F_c^2)^2] / \sum [w(F_o^2)^2]^{1/2}$ **References.**

- [1] G. C. Thaggard, K. C. Park, J. Lim, B. K. P. M. Kankanamalage, J. Haimerl, G. R. Wilson, M. K. McBride, K. L. Forrester, E. R. Adelson, V. S. Arnold, S. T. Wetthasinghe, V. A. Rassolov, M. D. Smith, D. Sosnin, I. Aprahamian, M. Karmakar, S. K. Bag, A. Thakur, M. Zhang, B. Z. Tang, J. A. Castaño, M. N. Chaur, M. M. Lerch, R. A. Fischer, J. Aizenberg, R. Herges, J.-M. Lehn, N. B. Shustova, *Nat. Commun.* **2023**, *14*, 7556.
- [2] M. J. Katz, Z. J. Brown, Y. J. Colón, P. W. Siu, K. A. Scheidt, R. Q. Snurr, J. T. Hupp, O. K. Farha, *Chem. Commun.* **2013**, *49*, 9449–9451.
- [3] J. Lim, K. C. Park, G. C. Thaggard, Y. Liu, B. K. P. M. Kankanamalage, D. J. Toler, A. T. Ta, P. Kittikhunnatham, M. D. Smith, S. R. Phillpot, N. B. Shustova, *J. Am. Chem. Soc.* **2024**, *146*, 12155–12166.

- [4] D. Samanta, D. Galaktionova, J. Gemen, L. J. W. Shimon, Y. Diskin-Posner, L. Avram, P. Král, R. Klajn, *Nat. Commun.* **2018**, *9*, 641.
- [5] APEX3 Version 2019.11-0 and SAINT+ Version 8.40B. Bruker AXS, Inc., Madison, Wisconsin, USA, 2019.
- [6] L. Krause, R. Herbst-Irmer, G. M. Sheldrick, D. Stalke, *J. Appl. Crystallogr.* **2015**, *48*, 3–10.
- [7] G. M. Sheldrick, *Acta Crystallogr. Sect. A* **2015**, *71*, 3–8.
- [8] G. M. Sheldrick, *Acta Crystallogr. Sect. C* **2015**, *71*, 3–8.
- [9] O. V. Dolomanov, L. J. Bourhis, R. J. Gildea, J. A. K. Howard, H. Puschmann, *J. Appl. Crystallogr.* **2009**, *42*, 339–341.
- [10] R. Friedman, *ChemPhysChem* **2023**, *24*, e202200516.
- [11] J. Tao, J. P. Perdew, V. N. Staroverov, G. E. Scuseria, *Phys. Rev. Lett.* **2003**, *91*, 146401.
- [12] V. N. Staroverov, G. E. Scuseria, J. Tao, J. P. Perdew, *J. Chem. Phys.* **2003**, *119*, 12129–12137.
- [13] B. P. Pritchard, D. Altarawy, B. Didier, T. D. Gibson, T. L. Windus, *J. Chem. Inf. Model.* **2019**, *59*, 4814–4820.
- [14] K. L. Schuchardt, B. T. Didier, T. Elsethagen, L. Sun, V. Gurumoorthi, J. Chase, J. Li, T. L. Windus, *J. Chem. Inf. Model.* **2007**, *47*, 1045–1052.
- [15] Gaussian 16, Revision A.03, M. J. Frisch, G. W. Trucks, H. B. Schlegel, G. E. Scuseria, M. A. Robb, J. R. Cheeseman, G. Scalmani, V. Barone, G. A. Petersson, H. Nakatsuji, X. Li, M. Caricato, A. V. Marenich, J. Bloino, B. G. Janesko, R. Gomperts, B. Mennucci, H. P. Hratchian, J. V. Ortiz, A. F. Izmaylov, J. L. Sonnenberg, D. Williams-Young, F. Ding, F. Lipparini, F. Egidi, J. Goings, B. Peng, A. Petrone, T. Henderson, D. Ranasinghe, V. G. Zakrzewski, J. Gao, N. Rega, G. Zheng, W. Liang, M. Hada, M. Ehara, K. Toyota, R. Fukuda, J. Hasegawa, M. Ishida, T. Nakajima, Y. Honda, O. Kitao, H. Nakai, T. Vreven, K. Throssell, J. A. Montgomery, Jr., J. E. Peralta, F. Ogliaro, M. J. Bearpark, J. J. Heyd, E. N. Brothers, K. N. Kudin, V. N. Staroverov, T. A. Keith, R. Kobayashi, J. Normand, K. Raghavachari, A. P. Rendell, J. C. Burant, S. S. Iyengar, J. Tomasi, M. Cossi, J. M. Millam, M. Klene, C. Adamo, R. Cammi, J. W. Ochterski, R. L. Martin, K. Morokuma, O. Farkas, J. B. Foresman, and D. J. Fox, Gaussian, Inc., Wallingford CT, 2016.
- [16] S. Grimme, J. Antony, S. Ehrlich, H. Krieg, *J. Chem. Phys.* **2010**, *132*, 154104.
- [17] S. Grimme, S. Ehrlich, L. Goerigk, *J. Comput. Chem.* **2011**, *32*, 1456–1465.
- [18] L. E. Aebersold, A. K. Wilson, *J. Phys. Chem. A* **2021**, *125*, 7029–7037.
- [19] L. Goerigk, S. Grimme, *J. Chem. Theory Comput.* **2011**, *7*, 291–309.
- [20] F. Neese, *Wiley Interdiscip. Rev.: Comput. Mol. Sci.* **2022**, *12*, e1606.
- [21] Y. Liu, A. T. Ta, K. C. Park, S. Hu, N. B. Shustova, S. R. Phillpot, *Microporous Mesoporous Mater.* **2024**, *364*, 112882.
- [22] Y. Liu, A. T. Ta, S. Pandey, K. C. Park, S. Hu, N. B. Shustova, S. R. Phillpot, *Comput. Mater. Sci.* **2023**, *230*, 112528.
- [23] A. V. Marenich, C. J. Cramer, D. G. Truhlar, *J. Phys. Chem. B* **2009**, *113*, 6378–6396.
- [24] J. Ho, A. Klamt, M. L. Coote, *J. Phys. Chem. A* **2010**, *114*, 13442–13444.
- [25] G. R. Choppin, M. P. Jensen, **2006**, 2524–2621.
- [26] N. Ko, J. Hong, S. Sung, K. E. Cordova, H. J. Park, J. K. Yang, J. Kim, *Dalton Trans.* **2014**, *44*, 2047–2051.
- [27] A. Perry, S. J. Green, D. W. Horsell, S. M. Hornett, M. E. Wood, *Tetrahedron* **2015**, *71*, 6776–6783.
- [28] M. Natali, L. Soldi, S. Giordani, *Tetrahedron* **2010**, *66*, 7612–7617.

**Author contributions.**

K. C. Park: data curation (lead), writing of original draft (lead), writing - reviewing and editing (supporting), investigation (lead), and formal analysis (lead)

J. Lim: data curation (supporting), writing - reviewing and editing (supporting), investigation (supporting), and formal analysis (supporting)

G. C. Thaggard: data curation (supporting), writing of original draft (supporting), and formal analysis (supporting)

B. K. P. Maldeni Kankanamalage: data curation (supporting), writing - reviewing and editing (supporting), and formal analysis (supporting)

I. Lehman-Andino: data curation (supporting), writing - reviewing and editing (supporting), and formal analysis (supporting)

Y. Liu: data curation (supporting), writing - reviewing and editing (supporting), and formal analysis (supporting)

C. R. Martin: data curation (supporting), writing - reviewing and editing (supporting), and formal analysis (supporting)

J. M. Burrell: data curation (supporting), writing - reviewing and editing (supporting), and formal analysis (supporting)

A. T. Ta: data curation (supporting), writing - reviewing and editing (supporting), and formal analysis (supporting)

A. B. Greytak: supervision (supporting), writing – reviewing and editing (supporting), formal analysis (supporting), resources (supporting)

J. W. Amoroso: supervision (supporting), writing – reviewing and editing (supporting), formal analysis (supporting), resources (supporting)

D. P. DiPrete: supervision (supporting), writing – reviewing and editing (supporting), formal analysis (supporting), resources (supporting)

M. D. Smith: data curation (supporting), formal analysis (supporting), crystallography (lead)

S. R. Phillpot: supervision (supporting), writing – reviewing and editing (supporting), formal analysis (supporting), resources (supporting)

N. B. Shustova: conceptualization (lead), funding acquisition (lead), project administration (lead), resources (lead), supervision (lead), formal analysis (lead), writing of original draft (lead), writing - reviewing and editing (lead)